Electro- and Photocatalytic Generation of Hydrogen by Iron Polypyridyl Complexes

Kathryn J. Mayer
College of William and Mary

Recommended Citation

Electro- and Photocatalytic Generation of Hydrogen by Iron Polypyridyl Complexes

A thesis submitted in partial fulfillment of the requirement
for the degree of Bachelors of Science in Department of Chemistry from
The College of William and Mary

By

Kathryn J. Mayer

Accepted for _Honors_

_____
William R. McNamara
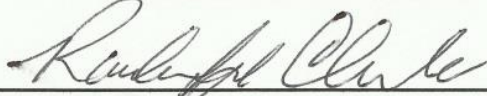
_____
Randolph Chambers
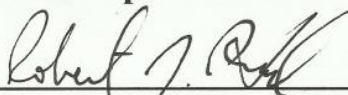
_____
Robert J. Hinkle
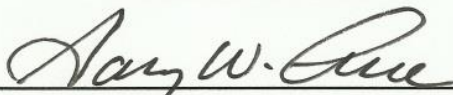
_____
Gary W. Rice

Williamsburg, VA
May 6, 2015

Table of Contents

Acknowledgements

I would like to thank Dr. William McNamara for his guidance over the last two years. You have helped me cultivate my skills as a scientist both in and out of the lab. Thank you for teaching me to think critically about chemical problems and to develop creative solutions to solve them. I would not be where I am today without your support.

Thank you to all of the wonderful chemistry professors I have had the pleasure to learn from at William and Mary over the past four years. My time here has been greatly shaped by your passion for knowledge and your dedication to your students. Thank you to Professor Hinkle for two excellent semesters of organic chemistry. A special thank you is due to Professor Rice for inspiring me to learn more about analytical chemistry during Instrumental Analysis last year and this semester in Advanced Analytical Chemistry. Both of your courses have greatly contributed to my decision to pursue a graduate degree in atmospheric chemistry.

I would like to thank Dr. Chambers for serving as my minor advisor in the Environmental Science and Policy Department. The ENSP classes I have taken at William and Mary have shaped my perspective on the complex relationship between humans and the environment. In the long-term, I hope to combine my interest in this subject with chemistry to help protect the health of the environment.

Thank you to the McNamara lab group for all of your support with this project. I would like to thank Gannon Connor for his role in developing the original FeNNNO complex. Without his hard work last year, this project would not have been possible. I would also like to thank Trevor Chang and Lexi Silva for their contributions to my project.

List of Figures and Tables

Figures:

Tables:

Appendix Figures:

Abstract

An iron polypyridyl complex has been synthesized, characterized, and shown to be both an electro- and photocatalyst for proton reduction. Electrochemically, the complex is active in both organic and aqueous solutions, with a reduction potential of -1.17 V vs SCE in CH_3CN. This corresponds to a thermodynamic overpotential of 660 mV. The activity of the complex increases in 1:1 H_2O/CH_3CN solvent conditions. Additionally, it has been found to work in aqueous buffer solutions at pH 3-5. It has also been found that the reduction potential of the complex can be tuned by adding electron withdrawing and donating groups to the ligand.

Photocatalytic hydrogen evolution has been observed by the same complex in the presence of fluorescein and triethylamine in 1:1 $EtOH/H_2O$ solutions, achieving 2400 turnovers with respect to catalyst over 24 hours.

Introduction

Climate Change

Since the mid-nineteenth century, a significant trend of global warming has been observed. The Earth's average surface temperature has increased 0.85 °C since 1880.[1] This warming trend has been correlated to a number of factors, such as greenhouse gas concentrations, aerosols, cloud cover, land use, and variations in solar irradiance.[1] Climate scientists have a high level of confidence that the largest contributions to global warming are the result of human activities, rather than natural events.[2] Anthropogenic contributors to climate change include the burning of fossil fuels, deforestation, and air pollution.
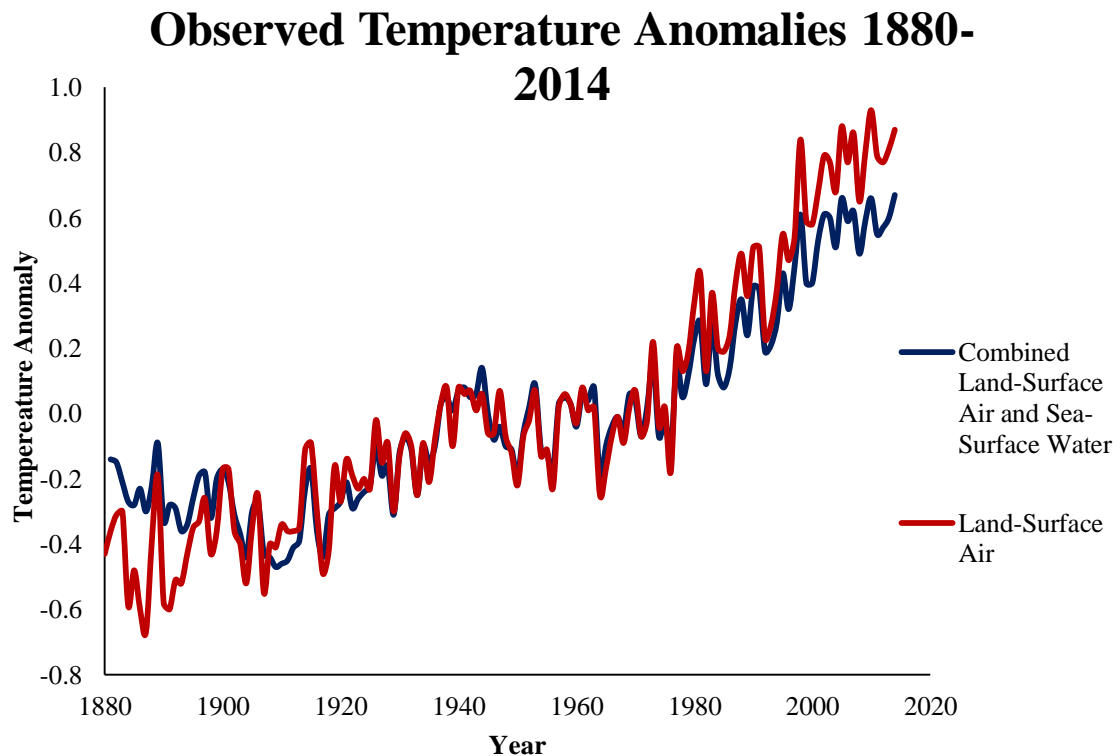
Figure 1. Observed temperature anomalies in the global annual mean temperature from 1880 to 2014[3]. The deviations are reported with respect to the average of the global annual mean temperatures from 1951 to 1980.

Greenhouse gases (GHGs) are atmospheric trace gases that make up less than one percent of the total atmosphere by volume. They include well-mixed gases such as carbon dioxide, methane, nitrous oxide, and halogenated carbon compounds, as well as short-lived species such as nitrogen oxide (NO_x) species, carbon monoxide, and volatile organic compounds. GHGs are distinct from other trace gases because they absorb and emit infrared radiation due to their IR active vibrational modes. Incoming solar radiation is mainly comprised of wavelengths in the UV, visible, and near IR range. Some of this radiation is naturally absorbed and reflected back into space by atmospheric gases like ozone or by cloud cover before it reaches the surface. The radiation which does strike the earth's surface is absorbed and emitted as thermal radiation in the far IR region. Because 99% of the atmosphere is IR transparent, most of this thermal radiation escapes back out into space. However, some of the radiation is absorbed by greenhouse gases and re-emitted back towards the earth's surface. This process leads to the warming of the lower atmosphere and is essential in regulating global surface temperatures.[4] Without the greenhouse effect, the earth would be much colder than it is today. Historical ice core data indicates that low levels of GHGs are correlated with ice ages, while higher concentrations correspond to warm periods.[1]
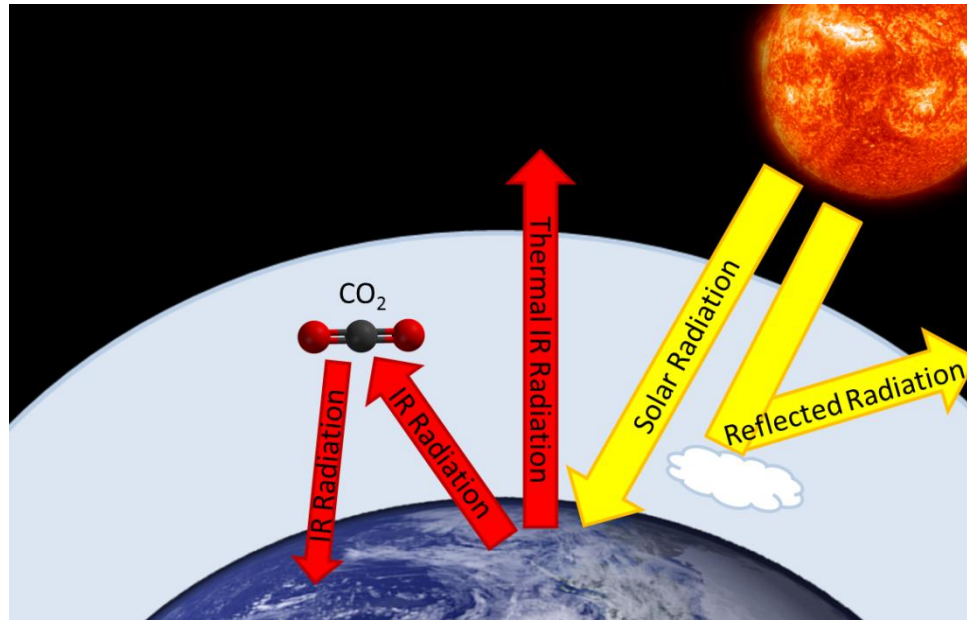
Figure 2. The greenhouse gas effect.

Carbon dioxide is the most common greenhouse gas and the largest contributor to global warming. It is naturally removed from the atmosphere by plants during photosynthesis and replenished by respiration of living organisms. Normally, the net flux of carbon in the atmosphere is relatively balanced and the atmospheric concentration of CO_2 remains constant, or if it does change, it happens very slowly. Ice core data shows that present day levels of carbon dioxide, methane, and nitrous oxide are the highest they have been during the past 800,000 years.[1] The rate of change is also alarming: the concentration carbon dioxide has increased from 280 ppm to over 400 ppm in less than two centuries, a 40% increase. The major source of this carbon imbalance is anthropogenic activities, namely the combustion of fossil fuels and deforestation.[5]

Monthly Atmospheric CO_2 Concentration 1958-2014
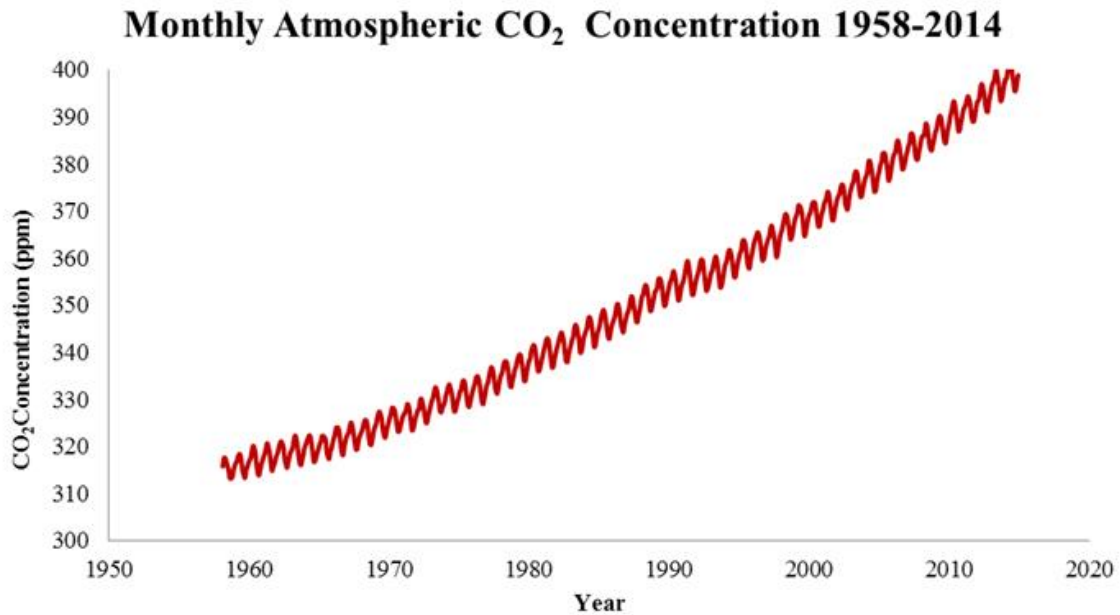
Figure 3. Monthly carbon dioxide concentrations measured in Mauna Loa, Hawaii between 1958 and 2014. The oscillating pattern is caused by seasonal variation. Data retrieved from the Scripps Institute of Oceanography CO_2 Project[6].

In addition to producing excess greenhouse gases and contributing to global warming, the combustion of fossil fuels can damage the environment and human health in other ways. Nitrogen oxide (NO_x) species and sulfur compounds, which are byproducts of combustion, react with water vapor in the troposphere to form nitric and sulfuric acid respectively and decrease the pH of rain water.[7] Acid rain damages soil and plants, as well as leading to increased fish mortality in affected ecosystems. Coal fired power plants are the single largest source of anthropogenic mercury emissions.[8] Mercury is a long-lived environmental toxin which bio-accumulates in high trophic level aquatic organisms, including many species of fish commonly consumed by humans.[9] The air pollution produced by automobiles and coal power plants is linked to human health issues, such as cancer, stroke, heart attack, asthma, and chronic obstructive pulmonary disease. The World Health Organization estimates that 2 million premature deaths are

caused by air pollution every year.[10] Increased concentrations of atmospheric CO_2 results in a higher concentration of carbonic acid in the oceans and causes them to become more acidic. Over the past century, the concentration of H^+ in the ocean has increased 26%, resulting in damage to shellfish, coral, and other calcifying organisms.[1]

Currently, most of the world's energy comes from the combustion of fossil fuels: coal, oil, and natural gas. These fuels store energy in carbon-carbon and hydrogen-carbon bonds and they release large amounts of carbon dioxide when they are burned. The combustion of fossil fuels is directly contributing to global warming, as well as other environmental issues such as acid rain, smog, and oil spills. Replacing them with clean, renewable energy sources would help solve numerous global problems ranging from economic insecurity to agricultural productivity[11] to health care costs. Experts from the World Health Organization's International Agency for Research on Cancer (IARC) have classified outdoor air pollution from anthropogenic sources as a human carcinogen and they have identified it as one of the leading contributors to lung and bladder cancers in developed countries[12].

In 2012, over 85% of the total energy consumed globally came from fossil fuel sources.[4] Only 8% of the total energy consumed was generated from renewable sources such as wind, solar, and hydroelectric power. This disparity is due to several factors, namely the high costs of renewable energy technology as well as the lack of infrastructure. For power plants entering service in 2019, the U.S. Energy Information Administration estimates that the cost of solar electricity generation will be 35% greater than for a conventional coal plant and almost twice as expensive as a natural gas-fired plant.[13] These statistics assume that the price of solar technology will continue to

decrease—the current costs of solar electricity generation are even higher. While wealthy developed nations in Europe and North America could adjust to these costs, the barriers for poorer countries to adopt renewable energy sources are much higher, making it necessary to develop lower cost options.

Global Energy Consumption by Source
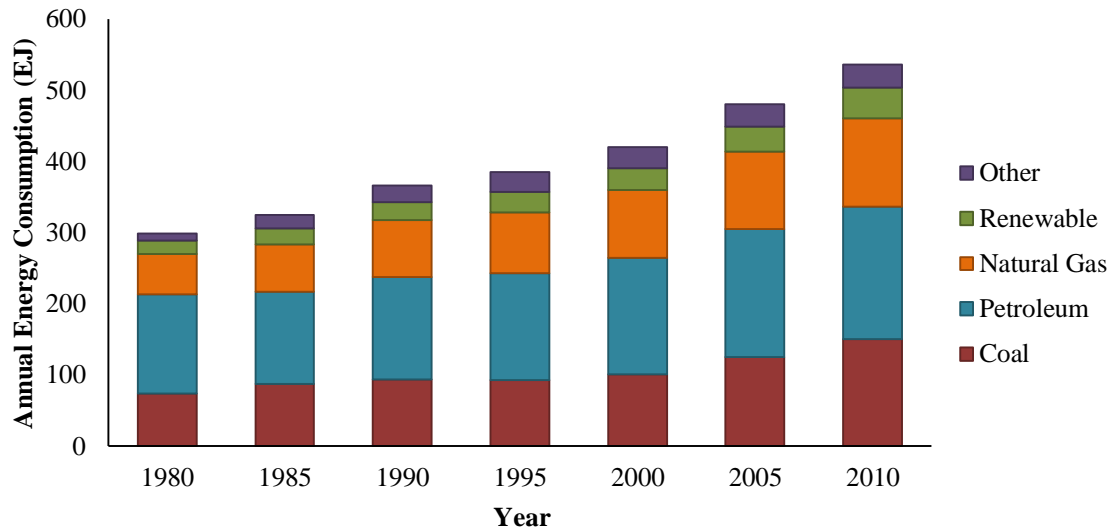
Figure 4. Global energy consumption broken down by source from 1980 to 2010.[14] Renewable refers only to electricity generation by sources such as solar, wind, and hydroelectric. Other includes biofuels, biomass, and nuclear.

In order to stabilize atmospheric greenhouse gas concentrations and prevent further damage to the earth, it is imperative that we phase out fossil fuel sources over the next few decades. Theoretically, renewable energy sources have the potential to replace fossil fuels several times over.[7] Enough solar energy strikes the earth in one hour to meet the entire year's global energy demands.[15] Even when accounting for factors such as device efficiency and land availability, the United States could have generated eleven times as much energy as it needed in 2012 using photovoltaics (Fig. 5).[9]

Unfortunately, there are several factors limiting the expansion of renewable energy sources. As discussed above, the cost of solar energy is very high compared to traditional sources; however, wind, hydroelectric, and geothermal are actually less expensive than coal power plants. Their biggest drawbacks are geographic: they can only be utilized in areas where the required natural resources such as rivers, adequate wind speeds, and thermal vents are found. These sources also have individual environmental drawbacks. Wind turbines kill a significant number of birds[16] and hydroelectric dams severely disrupt the habitats and migration patterns of aquatic organisms.[17] On the other hand, solar is a clean and universal energy source. It can be used to generate electricity almost anywhere on the planet.

Renewable Energy Potential Generation in the U.S.
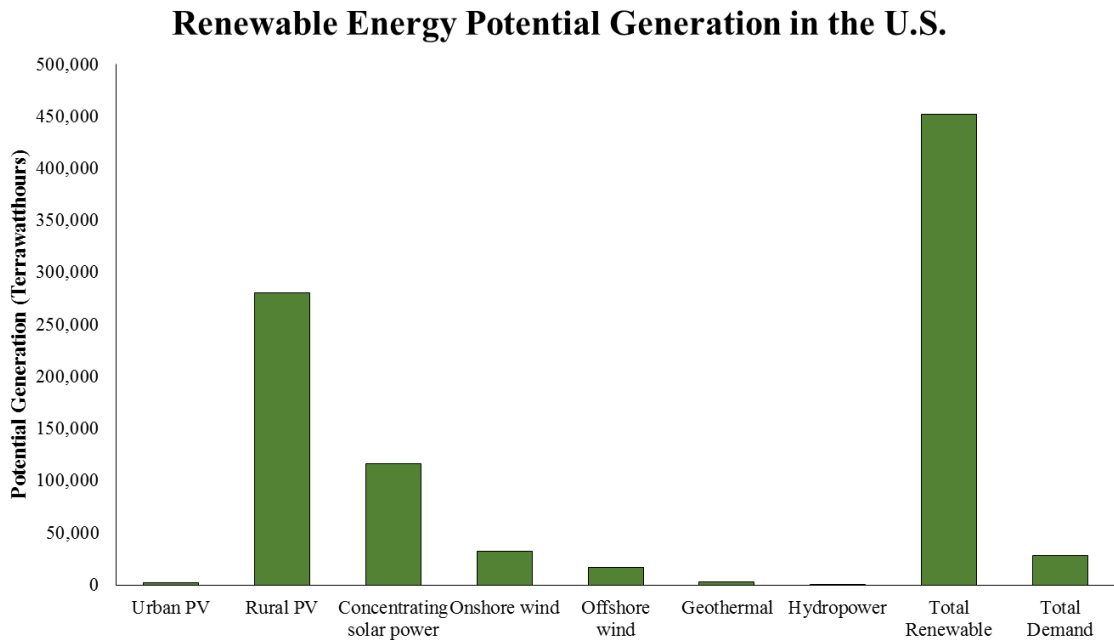
Figure 5. Potential generation of electricity by renewable of energy sources in the United States.[18]

The major drawback of solar energy is the diurnal variation of the sun. Electricity cannot be generated at night; thus, it is necessary to store energy during the daytime for

use later. In 2013, the average American home used 30 kWh of energy per day.[14] In order to store half of this energy, each household would go through 720 alkaline D batteries every night. High capacity batteries are an active area of research in chemistry and physics; however, they are hindered by difficulties such as efficiency, cost, and toxicity.[19]

Another strategy for energy storage is mechanical methods, the most popular of which is pumped-storage hydroelectric.[20] During peak production, excess energy is used to pump water up an elevation gradient and it is stored in a reservoir. The water is later released and
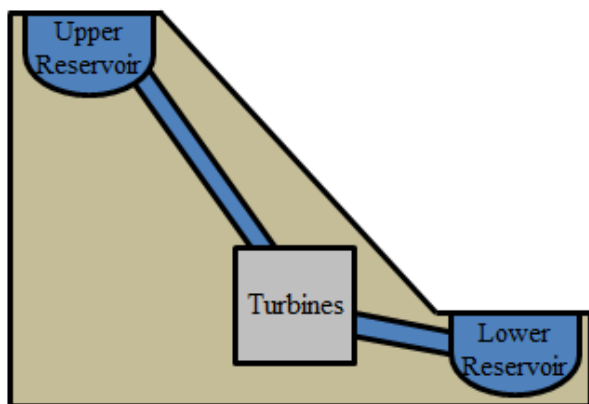
Figure 6. Schematic of a pump-storage hydroelectric system.

used to turn turbines as it flows downhill (Fig. 6). Although this is a mature and cost-effective method of energy storage, it is geographically constrained to areas which have an elevation change of several hundred meters and a large supply of fresh water. Pumped-storage hydroelectric also has a relatively low efficiency and it returns only 75% of the input energy back to the grid.

In natural systems, energy is stored in chemical bonds. During photosynthesis, plants utilize sunlight to convert carbon dioxide into high energy polysaccharides that can be stored and used later. Using nature as a model, several strategies have been proposed for chemical energy storage. The conversion of carbon dioxide into a fuel source is an attractive option; however, it presents significant thermodynamic and kinetic challenges.[21] The reduction of CO_2 to a useful molecule such as methanol or methane

14

typically involves several proton-coupled, multielectron steps, multiple catalysts, and a feedstock of hydrogen.

Another strategy for chemical energy storage is hydrogen generation via catalytic water splitting, sometimes referred to as artificial photosynthesis (AP). In this scheme, H_2O is oxidized to O_2 and H^+ by a catalyst and then the protons are reduced to H_2 using a second catalyst. The resulting hydrogen gas can be stored and then used later to generate electricity with a fuel cell, which produces only water as a byproduct (Fig. 7). Energy from renewable sources such as wind and solar photovoltaics can be stored by combining this method with electrocatalysts, or hydrogen can be generated directly from solar energy using photocatalytic systems.
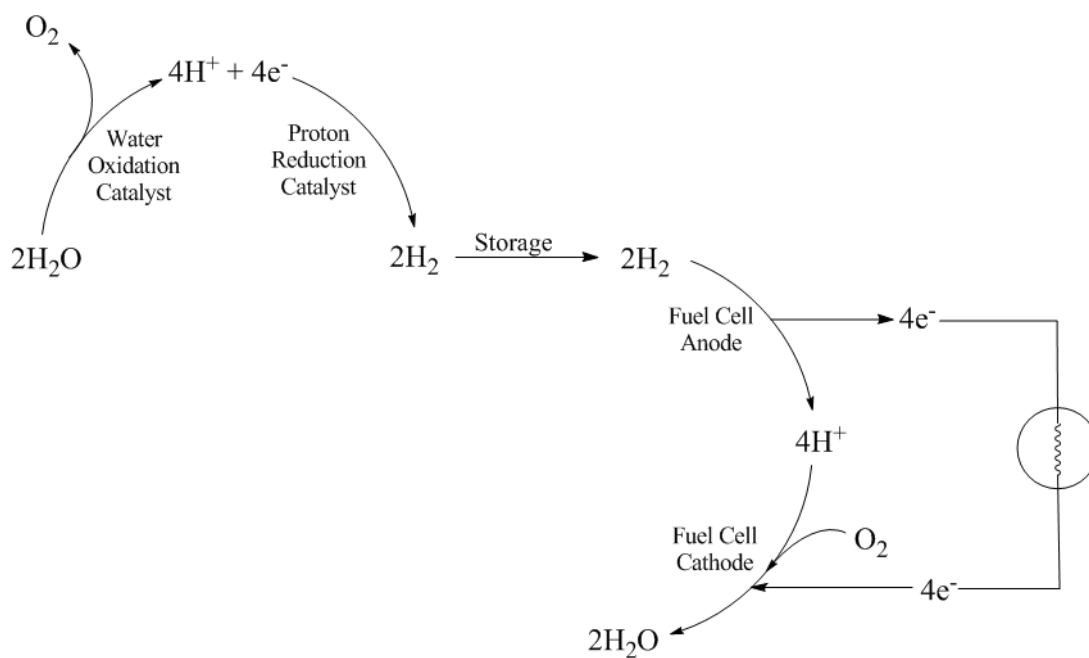
Figure 7. Hydrogen generation scheme for energy storage.

A major difficulty of implementing hydrogen as a fuel is storage. Although 1 kg of H_2 contains the same amount of energy as 3 kg of gasoline, the gaseous hydrogen

15

takes up 3,500 times more volume at standard temperature and pressure. Even when using compressed gas, a hydrogen fuel system for an automobile takes up more space and weighs more than an equivalent diesel system.[22] However, hydrogen fuel systems are both lighter and more compact than the lithium ion batteries used in electric cars. In addition to compressed gas, hydrogen can also be stored as a liquid or incorporated into a metal-hydride system for solid state storage.[23]

Photocatalytic Systems for Hydrogen Generation

Using a photocatalytic system for hydrogen generation is theoretically more efficient and cost effective than using electricity generated from renewable energy sources to split water. Although water oxidation is an active area of research in inorganic catalysis, this project focuses only on the reduction side of hydrogen generation. The absence of the oxidation half reaction necessitates the use of a sacrificial donor, which serves as a source of electrons to the system. A proton source is also needed. Depending on the experimental conditions, protons can be provided either by the addition of an acid or by simply using water in the solvent mixture. Rather than oxidizing water to produce protons, the system simply scavenges protons from the autodissociation of water.
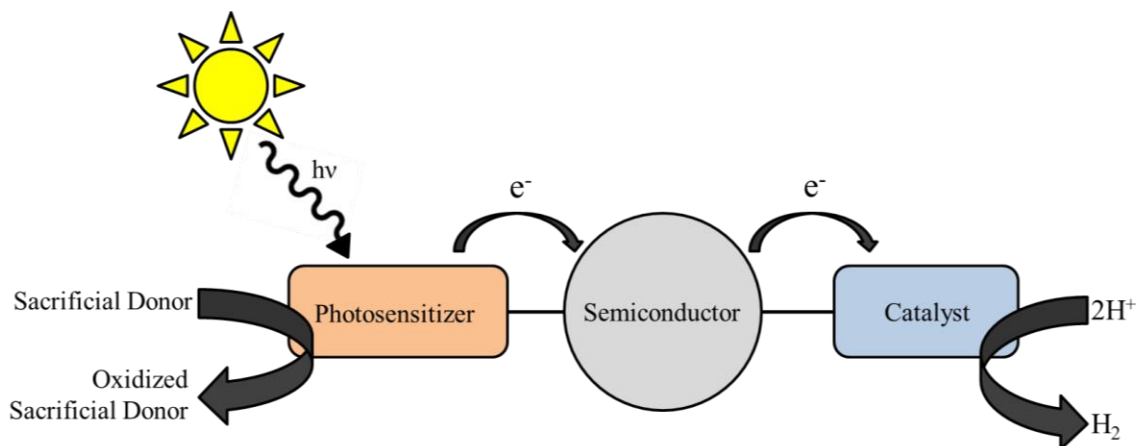
Figure 8. Proposed photocatalytic system for hydrogen generation consisting of a photosensitizer, a semiconductor, and a catalyst.

Heterogeneous systems for photocatalytic proton reduction typically contain three major components: a catalyst, a semiconductor, and a photosensitizer (fig. 8). Although it may work with just the free chromophore and catalyst in solution together, the system's efficiency will theoretically be much greater when these components are both bonded to a TiO_2 semiconductor. The semiconductor will eliminate the barrier of diffusion as well as aid with charge separation. From an industrial perspective, it also provides a solid material on which a device could be made.

The ultimate goal for photocatalytic proton reduction systems is to develop an industrial- scale method of energy storage. To be economically viable, it must be cost-competitive with other energy storage methods such as pump-storage hydroelectric and batteries. When designing these systems, it is necessary to consider a variety of factors including the cost, stability, and efficiency. Although highly active catalysts which use expensive metals like platinum and palladium are chemically interesting, they are not useful from a practical standpoint because of their prohibitively high costs. Ideal catalysts for water splitting use earth abundant metals like iron, copper, nickel, and

cobalt. In addition, using polydentate, chelating ligands improves the stability of the complexes. Another necessary quality of proton reduction catalysts is the ability to function in aqueous solutions. Many highly active, first row transition metal complexes decompose in water, making them unsuitable for these applications.

Experimental

Materials

All air-free syntheses were carried out using Schlenk techniques under an inert argon atmosphere. All chemicals were purchased from Fischer Scientific and were used without further purification.

Instrumentation

The ^{1}H NMR spectra for L_1 was recorded on a Varian Mercury 400VX spectrometer operating in the pulse Fourier transform mode. The spectra for L_2 was recorded on an Agilent 400MR DD2 spectrometer. Chemical shifts are referenced to residual solvent and coupling constants are reported in Hz. Elemental analyses of **1** and **2** were carried out by Atlantic Microlabs. High-resolution mass spectrometry was performed using positive electrospray ionization on a Bruker 12 Tesla APEX-Qe FTICR-MS with an Apollo II ion source. The electrochemical experiments were performed using a CH Instruments 620D potentiostat and a CH Instruments 680 amp booster. All experiments were carried out under an Ar atmosphere. Cyclic voltammetry was performed in a standard three-electrode cell using a glass carbon working electrode, a Pt auxiliary electrode, and an SCE reference electrode. The working and auxiliary electrodes were polished with alumina powder and rinsed before each experiment. Ferrocene was used as an internal standard to correct for reference electrode drift. Controlled potential coulometry was carried out using vitreous carbon working and counter electrodes and an Ag wire reference electrode in a closed, four-neck 500 mL flask. The electrodes were submerged into the solution and separated by vycor frits. Fluorescence spectroscopy was

performed on a Perkin-Elmer LS 55 Luminescence Spectrometer using a 4 mL screw-top quartz cuvette. UV-Vis experiments were performed using an Agilent Technologies Cary 60 UV-Vis spectrometer.   Photolysis experiments were carried out using a Newport 66902 Arc Lamp Housing with a Newport 69911 Power Supply with an Hg/Xe bulb operating at 200 watts. Gas analysis of the headspace was performed on a Bruker Scion 436 Gas Chromatograph equipped with a 2.0mm internal diameter packed column and a thermal conductivity detector (TCD). Ultra high purity Ar was used as the carrier gas.

X-ray Diffractometry

Data for **1** and **2** was collected on a Bruker-AXS three-circle diffractometer equipped with a SMART Apex II CCD detector using graphite-monochromated Cu Kα radiation (λ= 1.54 nm). SADABS was use to correct for Lorentz effects and absorption.   The structures were solved using direct methods and refined using the SHELXTL software package.

Syntheses
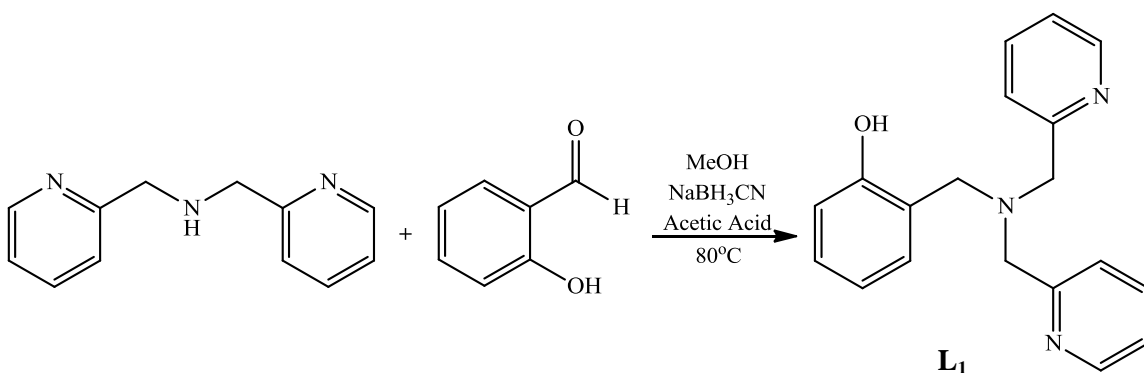
Figure 9. Scheme for synthesis of **L₁**.

N-(2-hydroxybenzyl)-N,N-bis(2-pyridulmethyl)amine (L₁). The ligand was synthesized using a modified literature procedure.[24] Salicylaldehyde (10 mmol) in 50 mL of methanol was degassed with Ar. To this, a degassed solution of bis(pyridine-2-ylmethyl)amine (10 mmol) in 10 mL of methanol was added. 3 drops of glacial acetic acid were added followed by the dropwise addition of a degassed solution of sodium cyanoborohydride (5 mmol) in 5 mL of methanol. The resulting clear, yellow solution was refluxed for 60 minutes, then stirred at room temperature overnight. The solution was acidified to pH 4 with 1 M HCl and it turned from yellow to amber. The solution was evaporated to dryness, then neutralized with 25 mL of saturated sodium carbonate (aqueous) and extracted with $CHCl_3$ (3 x 75 mL). The organic layer was dried with Na_2SO_4 and filtered through celite. The filtrate was evaporated to dryness, yielding an amber oil. The compound was purified through a silica gel column run sequentially in 99:1, then 19:1, then 9:1 DCM:MeOH. The purified product was collected at a yield of 59% (1.80g, 5.88 mmol). ^{1}H NMR ($CDCl_3$): δ 8.49 (d, 2H), 7.57 (t, 2H), 7.29 (d, 2H), 7.10 (m, 3H), 7.00 (d, 1H), 6.70 (t, 1H), 3.81 (s, 4H), 3.73 (s, 2H).
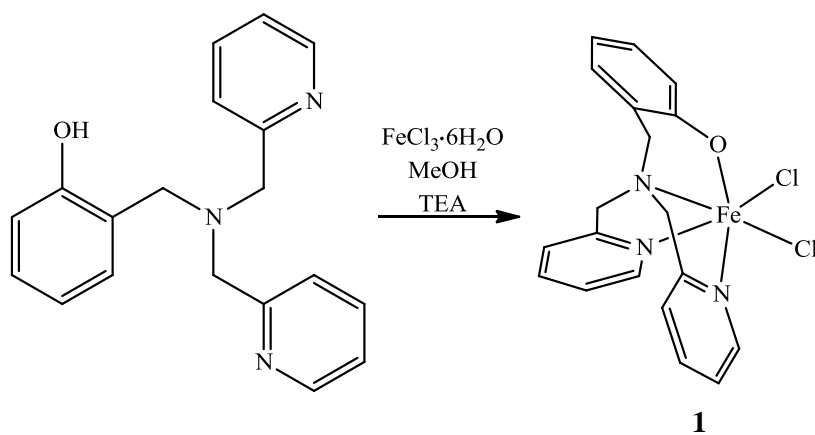
Figure 10. Synthesis of **1**

Fe-NNNO (1). Complex 1 was synthesized following a modified literature procedure. L_1 (5.88 mmol) and trimethylamine (4.7 mmol) were dissolved in 10 mL of MeOH and degassed with Ar. A solution of $FeCl_3 \cdot 6H_2O$ (4.7 mmol) dissolved in 10 mL of MeOH was degassed and the two solutions were combined under air-free conditions to yield a dark blue solution with a visible precipitate. The reaction was stirred for 1 hour and filtered, then the solid was washed with cold MeOH (3 x 10 mL). Complex **1** was collected at 74% yield (1.502 g, 3.48 mmol). The product was crystallized by diffusion of hexanes into a concentrated solution of **1** in DCM to yield blue feather crystals, which were collected by filtration. Crystals suitable for X-ray diffraction were grown by diffusion of diethyl ether into a concentrated solution of **1** in DCM. Anal. Calcd. for monohydrate $FeC_{19}H_{18}N_3Cl_2 \cdot H_2O$: C, 50.8; H, 4.49; N, 9.36%. Found: C, 50.66; H, 4.18; N, 9.13%. Expected m/z, 395.0482; found m/z, 395.0486.
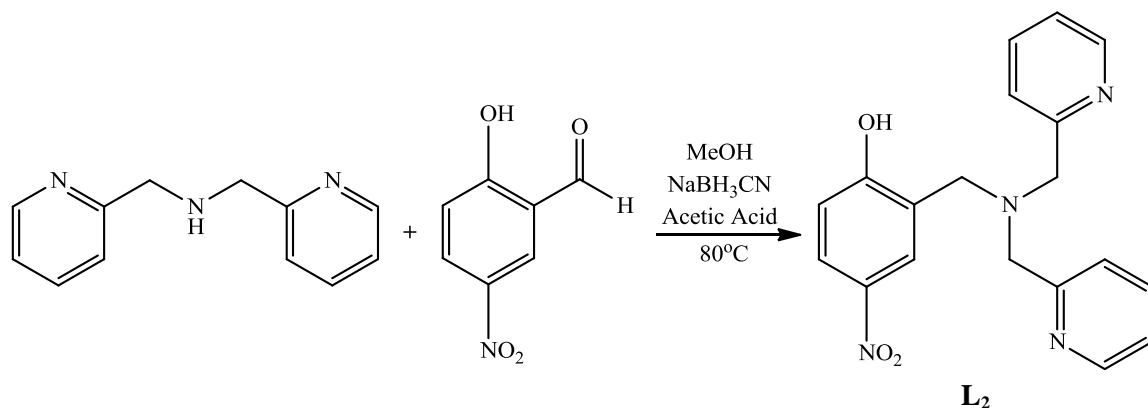
Figure 11. Scheme for synthesis of L_2.

N-(2-hydroxy-5-nitrobenzyl)-N,N-bis(2-pyridylmethyl)amine (L_2). The ligand was synthesized by the same procedure as L_1, but using nitro-substituted salicylaldehyde. 2-hydroxy-5-nitrobenzaldehyde (0.50 g, 3.0 mmol), was dissolved in 20 mL of MeOH and degassed with Ar. To this solution, a degassed solution of dipicolylamine (0.54 mL, 3.0 mmol) dissolved in 5 mL of MeOH was added. Then, 3 drops of glacial acetic acid

were added followed by the dropwise addition of a degassed solution of $NaBH_3CN$ (0.188g, 1.5 mmol) in 5 mL of MeOH. The dark orange solution was refluxed for 60 minutes and then stirred at room temperature for 72 hours. The solution was acidified to pH=4 with 1 M HCl and evaporated to near dryness and then neutralized with 30 mL of saturated Na_2CO_3 and extracted with 75 mL of chloroform. The organic layer was dried with $MgSO_4$ and filtered. The filtrate was evaporated to dryness to yield viscous orange oil. **L₂** was purified through a silica gel column run in 9:1 DCM:MeOH. The purified product was collected at a yield of 21% (0.21 g, 0.62 mmol). ^{1}H NMR (CDCl₃): δ 8.51 (d, 2H), 8.15 (d, 1H), 8.05 (s, 1H) 7.73 (t, 2H), 7.31 (t, 2H), 7.20 (d, 2H), 6.95 (d, 1H), 3.94 (s, 4H), 3.66 (s, 2H).
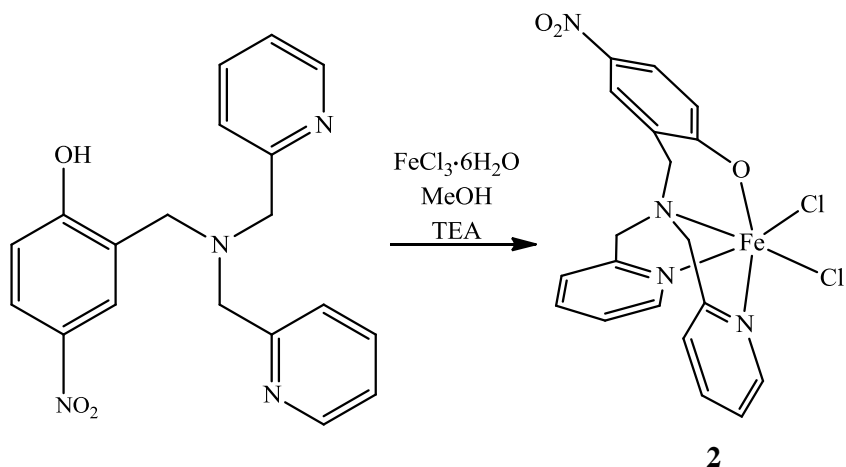
Figure 12. Synthesis of **2**

Fe-Nitro-NNNO Complex (2). Complex **2** was synthesized using the same procedure as **1** and collected at a 48% yield as dark purple crystals. Expected m/z, 497.992 ; found m/z, 497.992.

Controlled Potential Coulometry

Controlled potential coulometry (CPC) experiments were carried out in a sealed 500 mL four-necked flask. 3.0 mg of catalyst was added to 50 mL of aqueous buffer

solution. Vitreous carbon electrodes were used as the working and auxiliary electrodes and Ag wire was used as the reference. The electrodes were submerged in solution and separated by vycor frits. The flask was degassed with Ar, then 10 mL of gas was removed and 10 mL of CH_4 was added as an internal standard. The solution was stirred throughout the experiment. A CV was taken to identify the reduction potential. The CPC experiments were run at -1.2 V for 3600 seconds, then the headspace gas was analyzed by gas chromatography. The volume of H_2 evolved during the experiment was calculated using the ratio of the areas of the H_2 and CH_4 peaks. A calibration curve was prepared by adding known volumes of H_2 to a flask containing 50 mL of solution and 10 mL of CH_4, then taking a GC of the headspace. The following equation was obtained:

$$V_{H_2} = 0.5425 \times \left(\frac{Area_{H_2}}{Area_{CH_4}} \right) + 0.0198$$

Calibration Curve
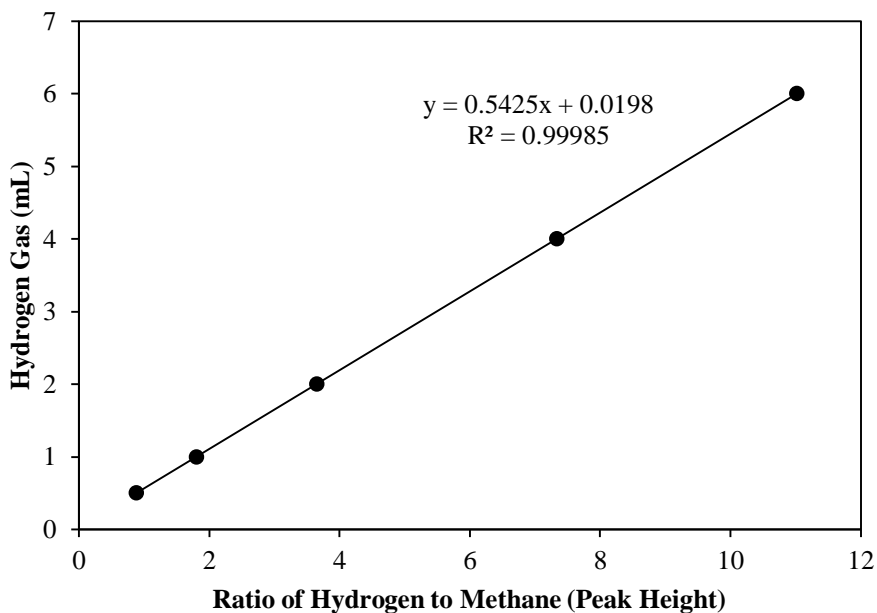
Figure 13. Calibration curve for CPC experiments. The ratio of the H_2 to CH_4 peaks is plotted versus the volume of H_2 in the flask.

Cyclic Voltammetry

Cyclic voltammetry experiments were carried out in 25x40 mm electrochemical cells using a three electrode system: glassy carbon was used for the working electrode, platinum for the auxiliary electrode, and a standard calomel electrode was used as the reference. The working and auxiliary electrodes were polished between runs with 0.05 μm alumina powder on a cloth polishing pad and then cleaned with H_2O and CH_3CN. Tertbutylammonium hexafluorophosphate (0.1 M) was used as the electrolyte in all experiments. For all experiments except the catalyst concentration study, a 0.5 mg portion of **1** or **2** was dissolved in 5 mL of solvent. For acid addition experiments, aliquots of 1.1 M TFA in CH_3CN were added to the cell using a Hamilton syringe. In the catalyst concentration study, TFA was diluted to volume with solvent in the cell and aliquots of a 25 mM stock solution of **1** in CH_3CN were added to it during the course of the experiment.

Photochemistry

Photolysis experiments were conducted in 16x125 mm glass test tubes sealed with size 17 rubber septa, which were secured with copper wire. Fluorescein and catalyst were added to the cells and diluted to 2.0 mL with ethanol. A stir bar was added, then the test tubes were capped and wrapped in aluminum foil to shield them from light. The test tubes were degassed with Ar for 5 minutes, then while Ar was still bubbling through the solution, 2.0 mL of a solution of trimethylamine (TEA) and water were slowly added through the septa with a syringe to give a total volume of 4.0 mL of 1:1 H_2O: EtOH. The test tubes continued to purge for 15 additional minutes. Using a Hamilton gastight

syringe, 1.0 mL of gas was removed from the test tubes and 1.0 mL of methane was added as an internal standard.
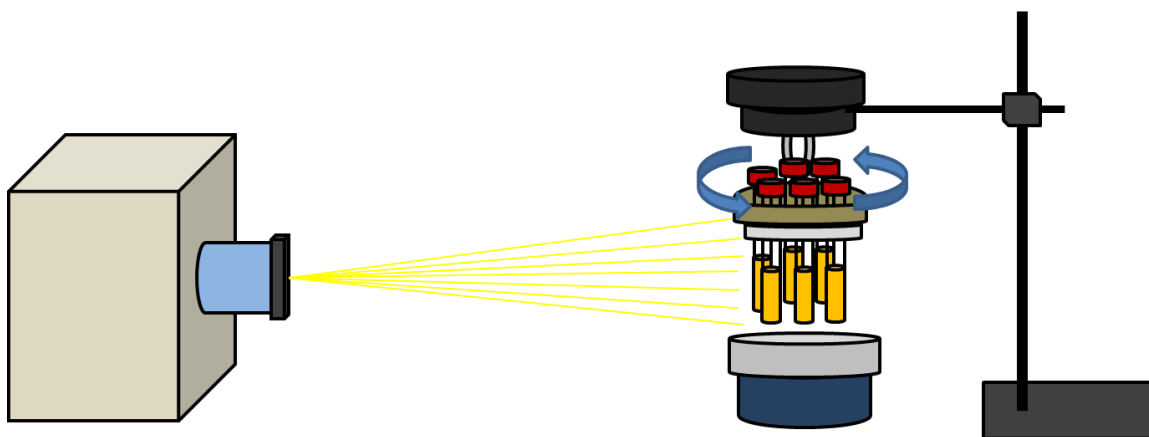
Figure 14. Schematic of photochemistry experimental set up, showing the arc lamp, test tube spinner, and stir plate.

Up to six samples were inserted into a custom-built test tube holder constructed from circular piece of plywood, styrofoam, and a small clip. The test tube holder was attached to a small motor which spins the samples at 3 revolutions per minute and positioned directly above a round stir plate. The samples were irradiated with light from an arc lamp for several hours. Hydrogen evolution was monitored by GC analysis. A 100 μL sample of the headspace gas was taken from the test tubes using a Hamilton gastight syringe and injected into the GC. The volume of hydrogen was determined using a calibration curve with methane as the internal standard.

Due to catalyst decomposition observed using the arc lamp, a new system which utilizes LEDs as the light source is under development. Preliminary results indicate that it will increase the yields of hydrogen obtained from the system. Strips of LEDs are attached to the outside of a 1000 mL beaker and the samples are spun inside with a motor

above a stir plate. A fan is used to cool the assembly. Green LEDs emitting at 520 nm are used with the fluorescein-FeNNNO system.

Photochemistry Calibration Curve

The retention times of hydrogen and methane were determined by injecting samples of those gases into the GC. Then, a photochemistry cell was prepared with 4.0 mL of 1:1 EtOH:H_2O, sealed, and degassed with Ar for 20 minutes. Using a gastight syringe, 1.0 mL of gas was removed from the test tube and replaced with 1.0 mL of methane. Then, a known volume of hydrogen was added to the cell and a 100 μL sample of the headspace gas was analyzed by GC. The resulting peaks were identified using their retention times and integrated to determine their respective areas. The volume of hydrogen added to the cell was plotted verses the ratio of hydrogen and methane peak areas, yielding the following equation:

$$V_{H_2} = 201.16 \times \left(\frac{\text{Area}_{H_2}}{\text{Area}_{CH_4}} \right)$$

Calibration Curve

$$y = 201.16x$$
$$R^2 = 0.9976$$

(Y-axis: Volume of H_2 (uL), X-axis: Area ratio)
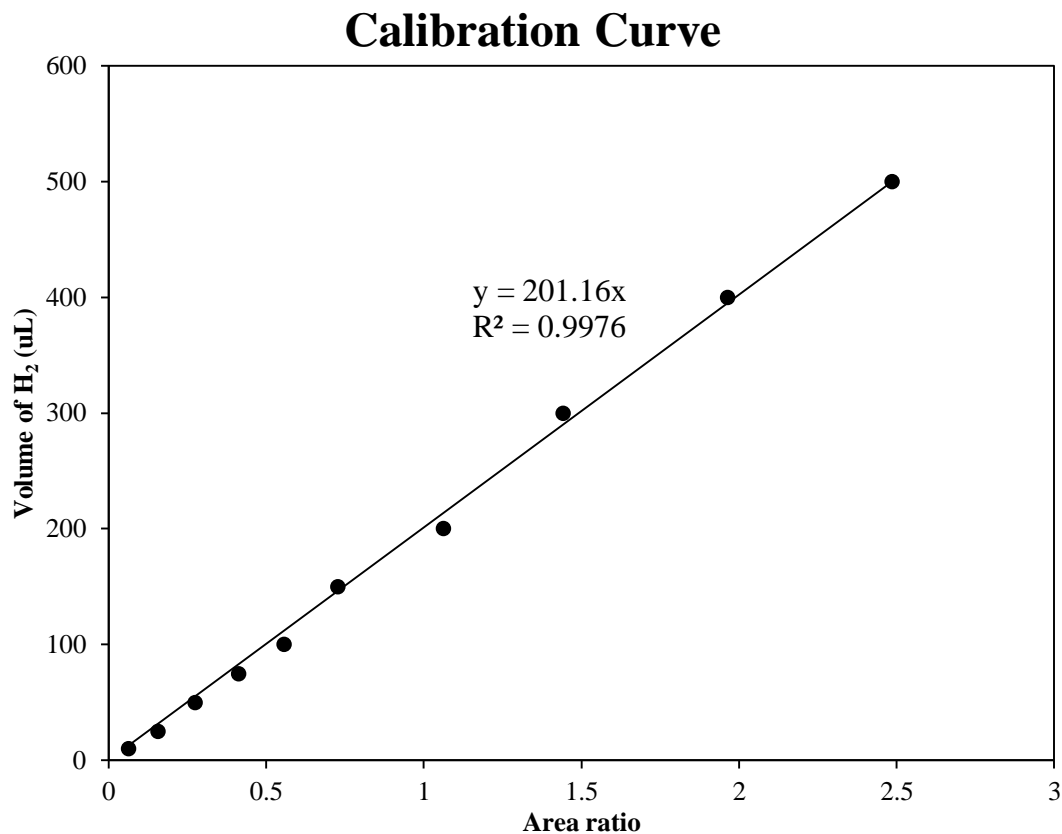
Figure 15. Calibration curve for photochemistry experiments. The volume of H_2 added to the test tubes is plotted verses the ratio of the areas of the H_2 and CH_4 peaks.

Fluorescence Quenching

Fluorescence quenching experiments were conducted in a 4 mL screw-top quartz cuvette with a cap equipped with a septum. The experiments were performed under Ar. A solution of fluorescein in a mixture of organic solvent and water was prepared in the cuvette. A solution of quencher (**1** or TEA) was prepared in a separate flask. The experiments scanned from 450 to 650 nm and used an excitation $\lambda = 430$ nm, a band gap of 5.0 nm, and a scan speed of 500 nm min^{-1}. A scan of the fluorescein solution was taken, then aliquots of the quencher were added and the cuvette was scanned again to measure changes in fluorescence intensity.

28

Results and Discussion

After synthesizing **1**, it was of interest to determine its molecular structure to verify that the desired product had been obtained. X-ray diffractometry was performed on plate crystals, which were grown by diffusing diethyl ether into a concentrated solution of **1** in dichloromethane. The resulting structure shows Fe(III) bonded to **L₁** through the three nitrogens and the phenol group, as well as to two chlorine
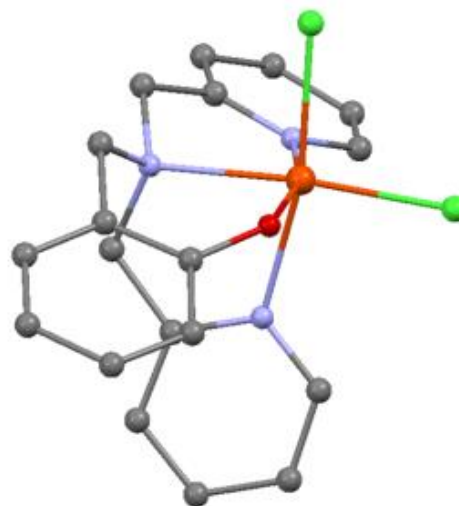
Figure 16. Crystal structure of **1**. Color code: Fe, orange; O, red; Cl, green; N, blue; C, black. Hydrogen atoms have been omitted for clarity.

atoms. The expected octahedral coordination sphere was found to have been distorted by the tetradentate ligand. The O-Fe-N and N-Fe-Cl bond angles were expected to be 180°, but they were determined to be 162.08°, 167.23°, and 166.99° respectively. The Fe-O bond length of 1.896 Å was shorter than other iron (III) phenolate bonds reported in the literature.[25] NMR spectroscopy could not be used for characterization because the Fe(III) complex has a d5 electron configuration and thus an unpaired electron, making it paramagnetic.

Electrochemistry

After the structure of **1** had been elucidated, it was of interest to assess its suitability as a proton reduction catalyst by performing electrochemical experiments. Cyclic voltammetry is a powerful technique for analyzing the redox activity of metal complexes. A potential is applied to the solution between the working and the reference electrodes, then it is swept from an initial potential to a more cathodic potential, then

back to the starting point. The cycle is performed at a constant rate, which is also referred to as the scan rate (V/s). The current enhancement is measured and plotted verses the applied potential. Redox events will appear as peaks in the resulting voltammogram. Both reversible and irreversible redox activity can be identified: reversible events will have corresponding reduction and oxidation peaks of the same size, whereas an irreversible process will only have a single peak. A reversible redox couple was observed at -0.28 V during cyclic voltammetry of **1** in CH_3CN without acid (Fig. 17). The top peak is a result of the reduction of Fe(III) to Fe(II), while the bottom peak shows the corresponding oxidation of Fe(II) back to Fe(III).
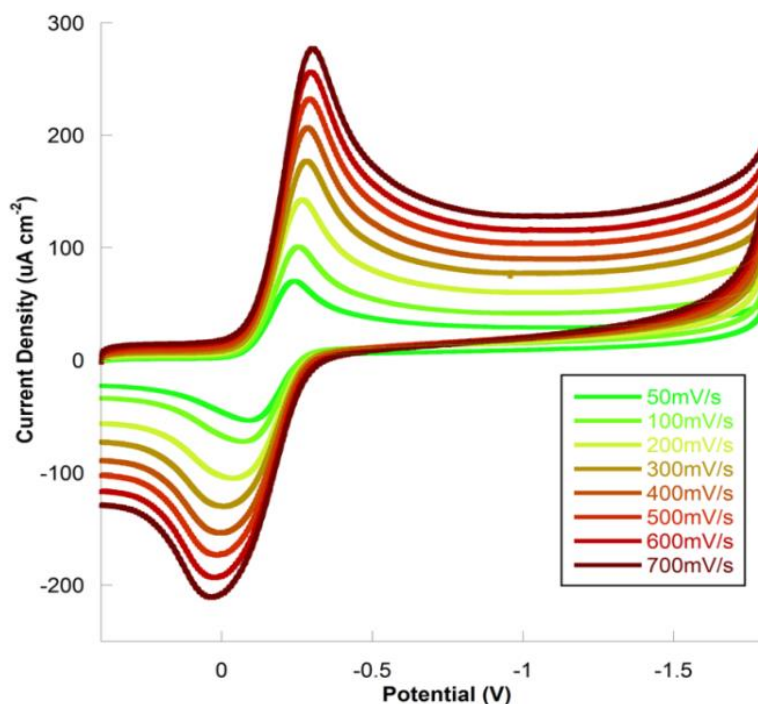
Figure 17. CVs of **1** in CH_3CN with 0.1 M TBAPF6 with no acid performed at various scan rates. The reversible redox couple which corresponds to Fe(II) being reduced to Fe(III) can be seen at -0.28 V.

To determine if complex **1** is capable of catalytically reducing protons, an acid addition experiment was performed. A CV was taken of **1** in CH_3CN and the reversible redox couple was observed at -0.28V. After the addition of trifluoroacetic acid, the

reversible redox couple shifted to -0.10 V and a new, irreversible reduction was observed at -1.17 V vs SCE (Fig. 18). Increasing the concentration of protons by adding additional aliquots of TFA caused the peak at -1.17 V to increase in current density, which indicates that the catalytic reduction of hydrogen is occurring at this potential.
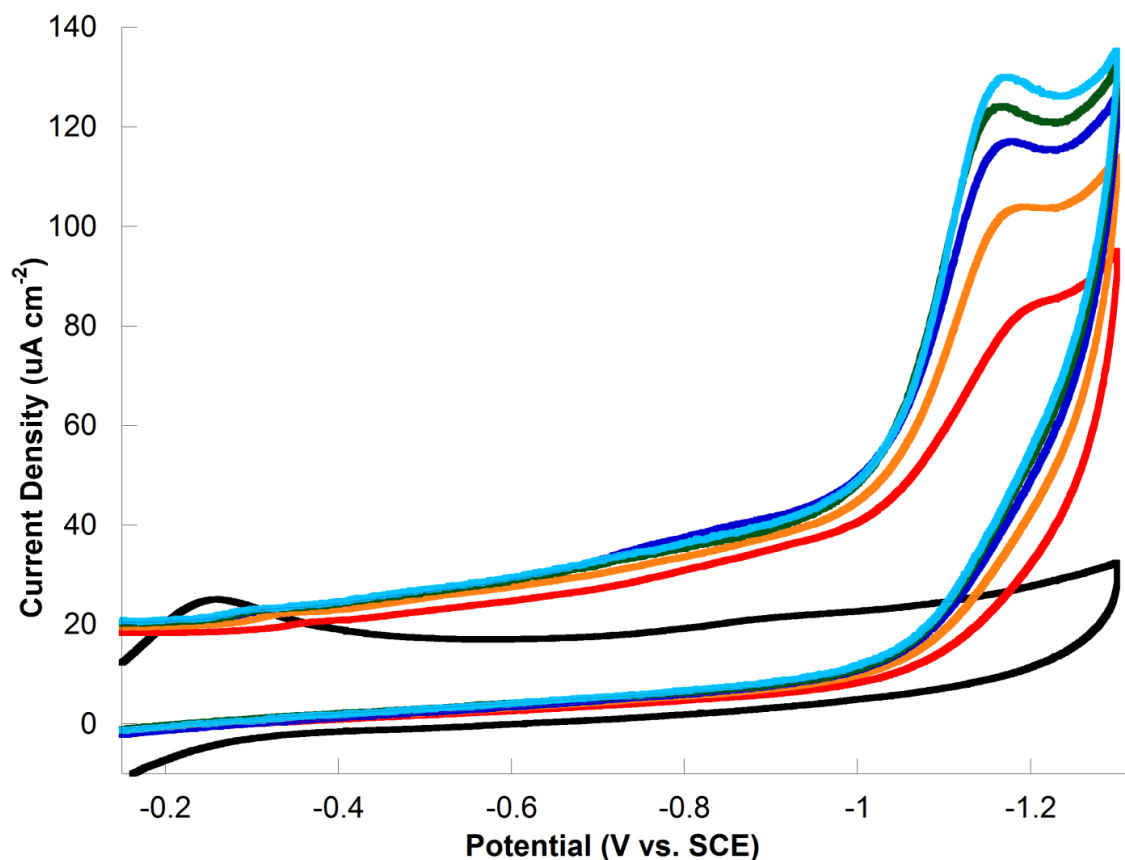
Figure 18. CVs of 0.5 mM **1** in CH_3CN with 0.1 M $TBAPF_6$ (black) upon addition of 2.2 mM TFA (red), 4.4 mM TFA (orange), 6.6 mM TFA (dark blue), 8.8 mM TFA (green), and 11.0 mM TFA (light blue) at a scan rate of 200 mV s^{-1}.

The cyclic voltammetry of **1** gives insight to the catalytic mechanism at work during proton reduction. Steps in the mechanism are classified as chemical (C) and electrochemical (E). Because the reduction of protons is a two electron process, four steps are expected. When acid is added, the original redox couple shifts. This indicates that the first step is a chemical transformation, which is believed to be the protonation of

the phenolate. The next step is the one-electron reduction at -1.17 V. There is no corresponding oxidation, which indicates that the species is chemically regenerated. The remainder of the catalytic mechanism is more difficult to deduce; however, it is suspected to proceed via a CEEC mechanism or a CECE mechanism.

Cyclic voltammetry can be used to determine the activity of a catalyst by measuring the current enhancement during a redox event. Activity is reported in terms of the i_c/i_p, which is the ratio of the current enhancements at the initial potential and at the catalytic potential. A complex is considered to be catalytic if the current enhancement at the reduction potential with a proton source present (i_c) is at least four times greater than the reduction potential of the complex with no proton source (i_p). For an iron complex, **1** is highly active with an i_c/i_p of 7.8 in CH_3CN.
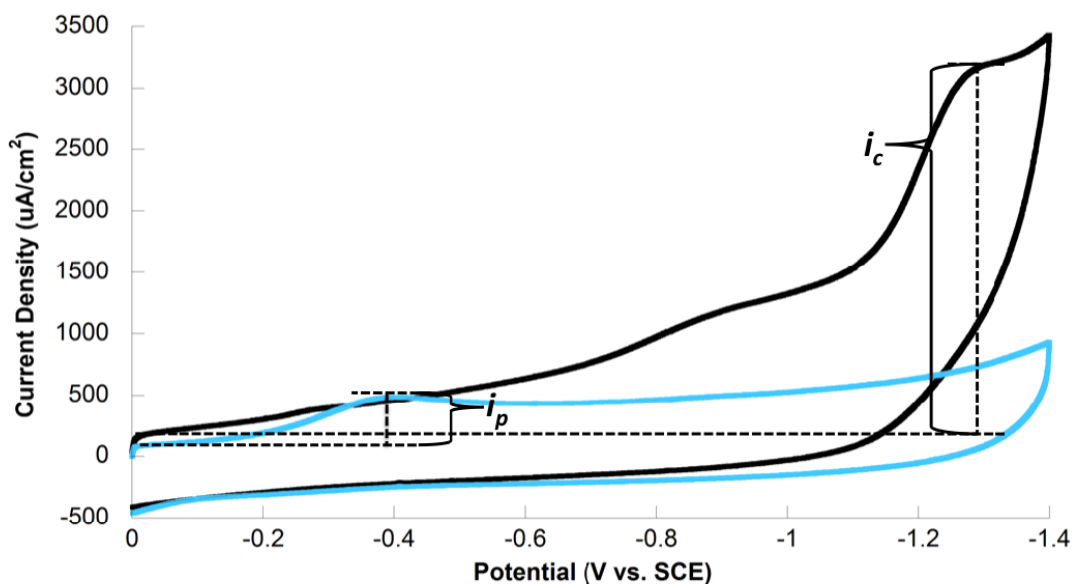
Figure 19. Determination of i_c and i_p data from cyclic voltammetry. CVs of **1** in CH_3CN were taken before (blue) and after (black) the addition of 26.4 mM TFA in the presence of 0.1 M TBAPF$_6$. Scans were taken at a rate of 10 V/s.

With the long-term goal of developing a system for generating hydrogen from the splitting of water molecules, it is of interest to develop of catalyst which is active in water as a solvent. In 1:1 H_2O/CH_3CN, it was observed that the i_c/i_p increases to 15.6 after correcting for background current. This shows that the complex actually becomes more active when water is added. In addition, a series of experiments were carried out in aqueous buffer solutions which showed that catalysis occurs in just water at an acidic pH.
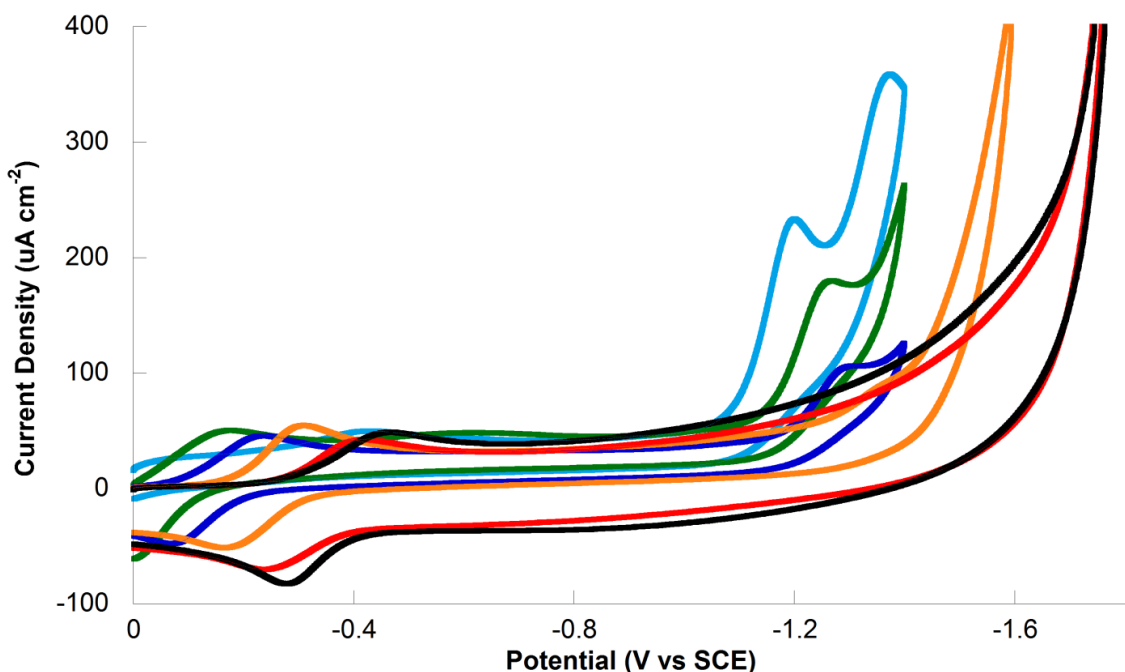
Figure 20. CVs of 0.5 mM **1** in citrate-buffered aqueous solutions at pH 3.0 (light blue), 4.0 (green), 5.0 (dark blue), 6.0 (orange), 7.0 (red), 8.0 (black) at a scan rate of 200 mV s^{-1} with a glassy carbon working electrode.

In order for a catalyst to be energetically efficient, it should operate at a potential which is close to the thermodynamic reduction potential of the substrate to minimize energy waste. The amount by which the catalytic potential exceeds the thermodynamic potential is referred to as the overpotential. In the literature, the thermodynamic reduction of protons from TFA in acetonitrile was determined to occur at -0.68 V vs

ferrocene.[26] The overpotential can be calculated by taking the difference between the experimentally determined catalytic potential and thermodynamic potential. The overpotential for **1** in CH_3CN was calculated to be 660 mV vs SCE. This is comparable to the literature values for other iron catalysts, although in organic solvents overpotentials as low as 300 mV have been reported.[27]

In addition to determining the overpotential, it was also of interest to calculate the rate of catalysis. Good catalysts are not only energetically efficient; they must also be fast. A catalyst concentration experiment was performed with **1** to determine the order of the reaction with respect to catalyst. Cyclic voltammograms were taken after aliquots of **1** were added to a cell containing 1:1 CH_3CN/H_2O and 44 mM TFA. When the peak current density was plotted versus the concentration of **1**, a linear relationship was observed. This indicates that the reduction of protons is first order with respect to catalyst.
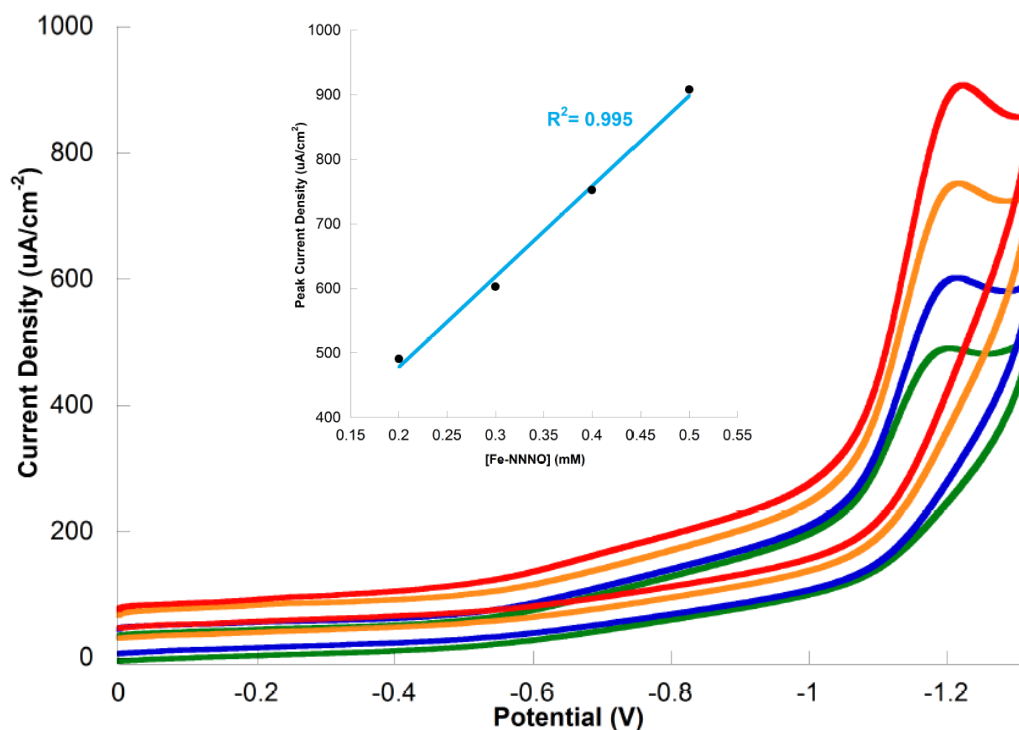
Figure 21. CVs of 5 mL 1:1 H_2O/CH_3CN solution containing 44 mM TFA scanned from 0.0 to -1.32 V at 200 mV/s with 0.2 mM (green), 0.3 mM (blue), 0.4 mM (orange), and 0.5 mM (red) **1** added in the presence of 0.1 M TBAPF$_6$. A graph of peak current density vs [**1**] is inlayed. The linear relationship indicates a first order dependence on catalyst.

Although **1** is highly active, it operates at a moderately high overpotential. It is desirable to develop catalysts with lower overpotentials to increase efficiency. The addition of electron withdrawing groups (EWG) to the ligand was expected to produce a catalyst with a lower reduction potential due to the decreased electron density around the metal center. Complex **2** is identical to **1**, except that is has a nitro group attached to the ligand. NO_2 functional groups are strongly deactivating and serve as good EWGs. Cyclic voltammetry of **2** in acetonitrile showed a reversible redox couple at -0.09 V vs SCE (fig. 20). Upon the addition of TFA, a catalytic wave was observed at -0.72 V, which corresponds to an overpotential of 210 mV vs SCE. This is significantly lower than **1**,

which operates at an overpotential of 660 mV. However, a decrease in activity was observed with the $i_c/i_p = 5.67$ in CH$_3$CN for **2**.
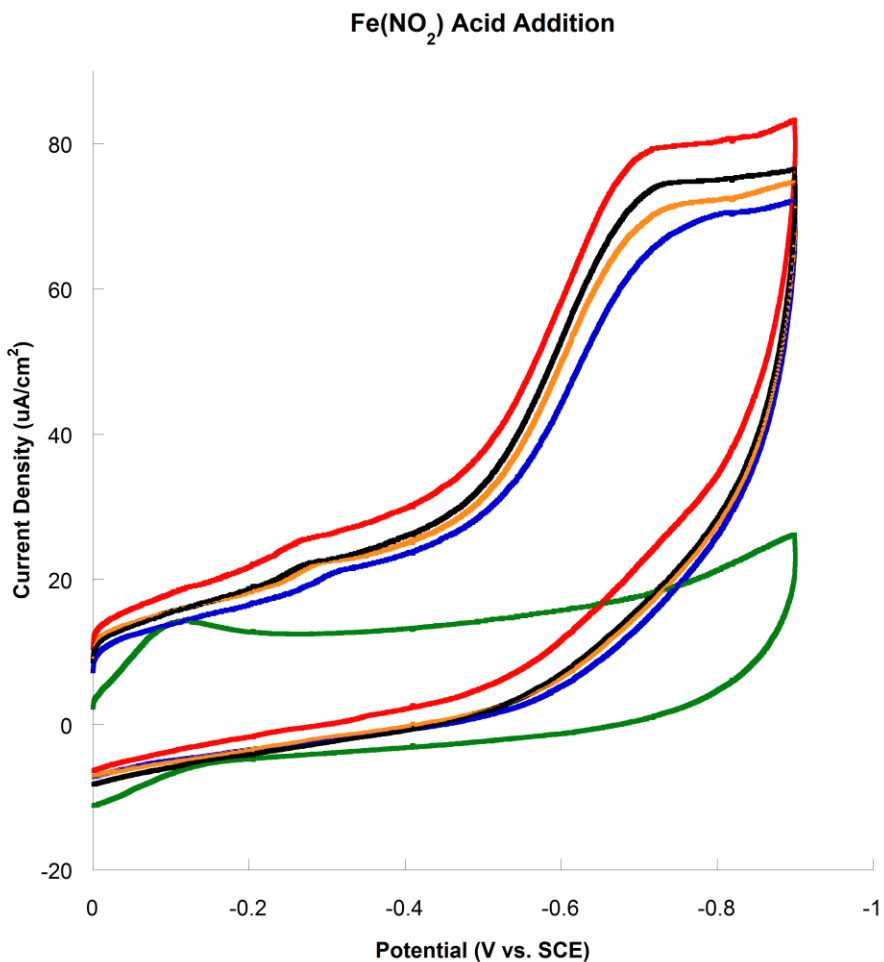
Figure 22. CVs of **2** in CH$_3$CN with 0.1 M TBAPF$_6$ (green) upon addition of 2.2 mM TFA (blue), 4.4 mM TFA (orange), 6.6 mM TFA (black), and 8.8 mM TFA (red) at a scan rate of 200 mV s^{-1}.

In order to confirm that **1** was electrocatalytically reducing protons to hydrogen, controlled potential coulometry experiments were performed. In these experiments, a solution of catalyst is held at the catalytic potential for proton reduction in the given solvent conditions for a set amount of time and the accumulation of charge is measured. At the end of the experiment, the headspace gases are analyzed by gas chromatography to quantify the hydrogen evolved. Hydrogen evolution by **1** was observed in aqueous buffer

36

solutions adjusted to pH=3-5. In a pH 5 solution, 23.0 equivalents of hydrogen were generated with respect to catalyst after one hour (Fig. 23). A control experiment without **1** was run to verify that the hydrogen evolution was the product of catalysis and not the result of the electrolysis of water by the electrodes.
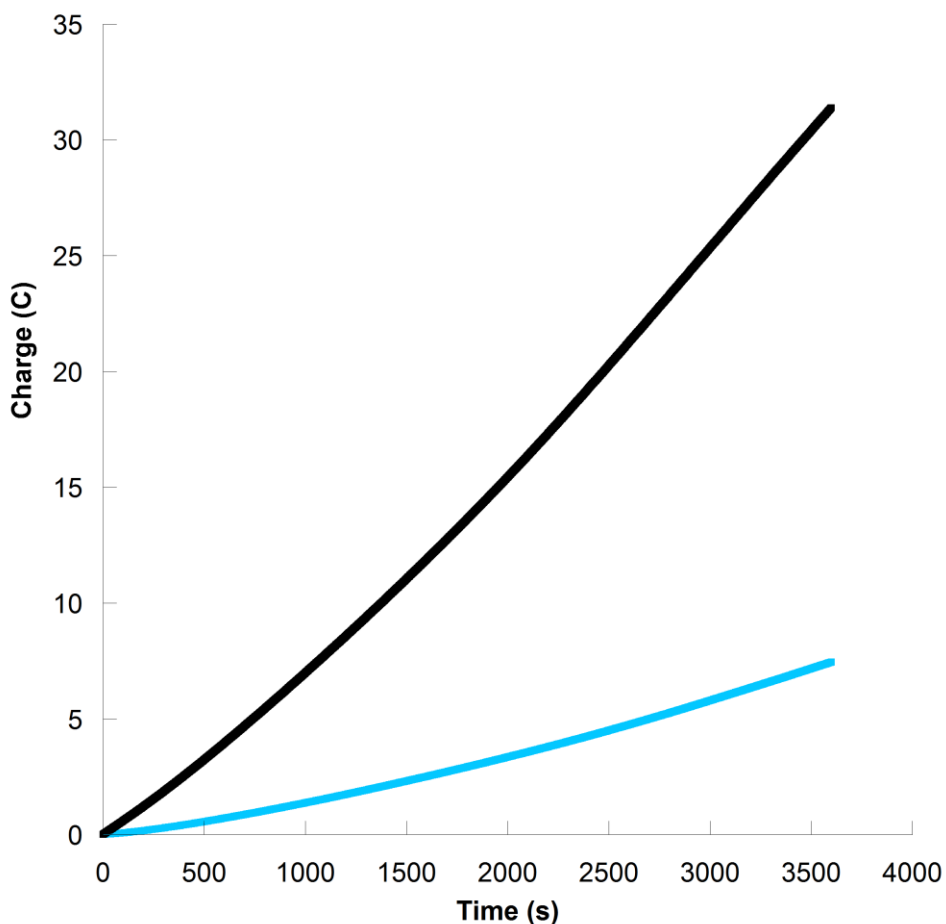
Figure 23. Controlled potential coulometry of **1** (0.139 mM) in 50 mL of aqueous buffer solution at pH=5 (black) and a control containing no catalyst (blue) at -1.2V for 3600 seconds.

The CPC experiment demonstrated that the catalytic wave observed at -1.2V is the result of the reduction of protons to hydrogen gas, rather than some other electrochemical event. In addition, CPC can be used to determine the faradaic efficiency of the system. The faradaic efficiency is efficiency with which charge is transferred

within an electrochemical system. It may be diminished by the production heat or by unwanted side reactions. The faradaic efficiency of **1** was determined by comparing the moles of H_2 produced to the moles of electrons put into the system. It was calculated to be 98%, which indicates that most of the electrons put into the system are being utilized in the reduction of protons, rather than contributing to other events.

Photochemistry

The results of the electrochemistry experiments indicated that **1** would be well-suited for use in a photochemical system for hydrogen generation. In addition to being highly active, **1** also functions in aqueous solutions. Hydrogen evolution was observed when solutions of **1** were irradiated with light in the presence of fluorescein and triethylamine (TEA). Fluorescein was selected because it has a relatively cathodic reduction potential of -1.7 V, which matches well with the catalytic potential of **1**. After 24 hours, 2,400 equivalents of H_2 with respect to catalyst were observed. This is comparable with other noble metal free systems reported in the literature.[28]

Hydrogen evolution by photcatalytic systems is often discussed in terms of the turnover numbers (TON), rather than the volume of hydrogen produced. The TON is the ratio of hydrogen evolved to catalyst in solution and it can be determined using the following equation:

$$\text{TON} = \frac{\text{moles of } H_2}{\text{moles of catalyst}}$$

Discussing hydrogen evolution using TONs allows the activity of different catalytic systems to be easily compared. For applications to energy storage, it is desirable to develop systems with high TONs because it indicates that the system is stable, active, and

long-lived. Noble-metal free systems which achieve several thousand turnovers in a 24 hour period have been reported in the literature.[30,31]

Interestingly, very little hydrogen evolution was observed in systems employing ruthenium-tris(2,2'-bipyridine) as the photosensitizer and ascorbic acid as the sacrificial donor. $Ru(bpy)_3^{2+}$ is more stable than fluorescein due to its long fluorescence lifetime. Unlike the relatively stable inorganic dyes, organic dyes can decompose via a photobleaching mechanism[29], which limits the useful lifetime of the photocatalytic system. It is suspected that the $Ru(bpy)_3^{2+}$ system did not perform well because it is not as reducing as fluorescein and **1** operates at a fairly negative catalytic potential. No hydrogen evolution was observed in a system containing Eosin Y as the chromophore and triethanolamine as the sacrificial donor. All samples appeared completely bleached after one hour, which indicates that the chromophore had decomposed.
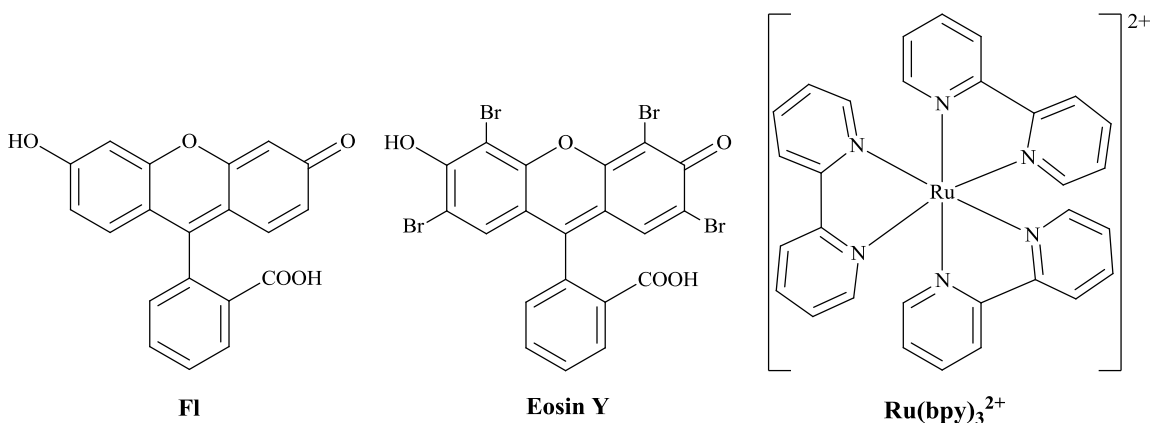
Figure 24. Chromophores tested in photocatalytic system with **1**: Fluorescein (left), Eosin Y (center), Ruthenium-tris(2,2'-bipyridine) (right).

Under high concentrations of TEA, the FeNNNO-fluorescein system is highly active; however, the samples frequently photo-bleach and system lifetime decreases. This is due to the reductive quenching of the excited fluorescein molecule, which

produces an unstable fluorescein anion and leads to decomposition of the system (Fig. 25). Low concentrations of TEA and high concentrations of catalyst can be used to force the system through an oxidative quenching pathway. Under these conditions, the system is more stable because electron transfer does not proceed via the unstable fluorescein anion.

$$Fe^{III}_{(cat)} + H^+ \rightleftharpoons Fe^{III}H \qquad Fe^{II}H \xrightarrow[+e^-]{+H^+} \mathbf{H_2} + Fe^{III}_{(cat)} \qquad TEA^+$$

Decomposition

Fl

TEA

Fl$^-$

Fl$^+$

Reductive Quenching

^{1}Fl*

Oxidative Quenching

TEA$^+$

TEA

$$Fe^{III}_{(cat)} + H^+ \rightleftharpoons Fe^{III}H \qquad Fe^{II}H \xrightarrow[+e^-]{+H^+} \mathbf{H_2} + Fe^{III}_{(cat)}$$
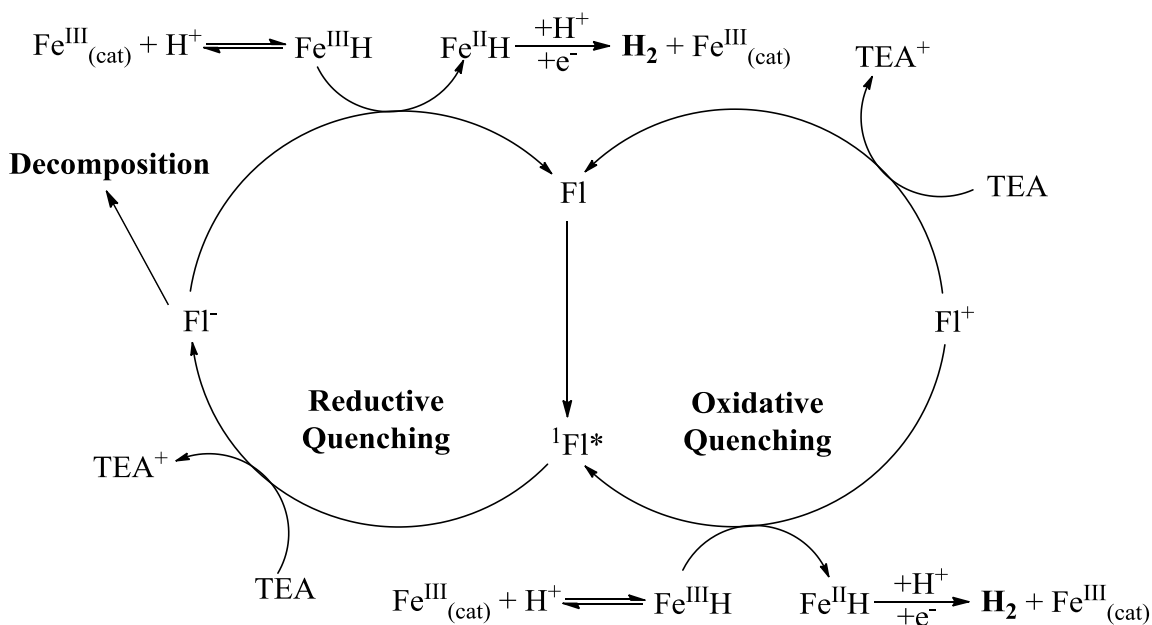
Figure 25. Reductive and oxidative quenching pathways of fluorescein during proton reduction by **1**.

In addition to TEA concentration, the activity of the photosystem is also dependent on chromophore concentration, catalyst concentration, and pH of the solution. In studies using the arc lamp, the distance of the samples from the lamp greatly affected hydrogen evolution. It is suspected that this is due to the changes in light intensity. In addition, temperature played a key role in the system activity—if the samples were positioned too close to the lamp, they began to heat up and the activity of the system was diminished. Hydrogen production increased dramatically when LEDs were used as the

excitation source, presumably due to the increased intensity of the light source. In addition, the LEDs did not significantly warm the samples.

The TEA-fluorescein system is very sensitive to changes in pH. At low pH, activity diminishes despite the higher concentrations of protons. It has been suggested that this is due to the protonation of TEA, which reduces its ability to serve as an electron donor.[30] Conversely, at very high pH, the low proton concentration impedes the generation of molecular hydrogen. It was found that the photocatalytic system performed best at pH 12. This observation is consistent with other fluorescein systems reported in the literature.[31]
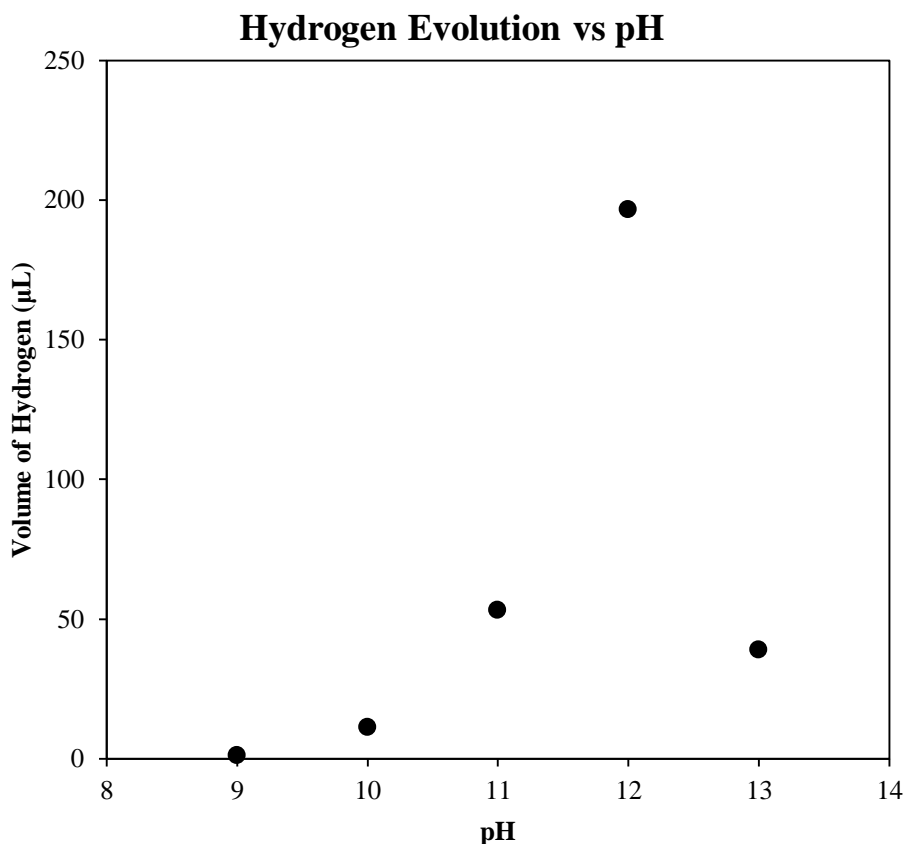
Figure 26. Volume of H_2 evolved by photolysis experiments containing **1** (1×10^{-5} M), fluorescein (1.0 mM), and TEA (5% v/v) in 1:1 EtOH/H_2O adjusted to various pH using HCl or NaOH.

To assess the rate of hydrogen evolution throughout the lifetime of the photocatalytic system, a photolysis experiment was run for 70 hours and GCs were taken periodically to monitor hydrogen evolution (Fig. 27). The rate of hydrogen evolution stayed constant throughout the experiment and it was calculated to be 34 turnovers per hour.

H$_2$ Evolution vs Time

R² = 0.994
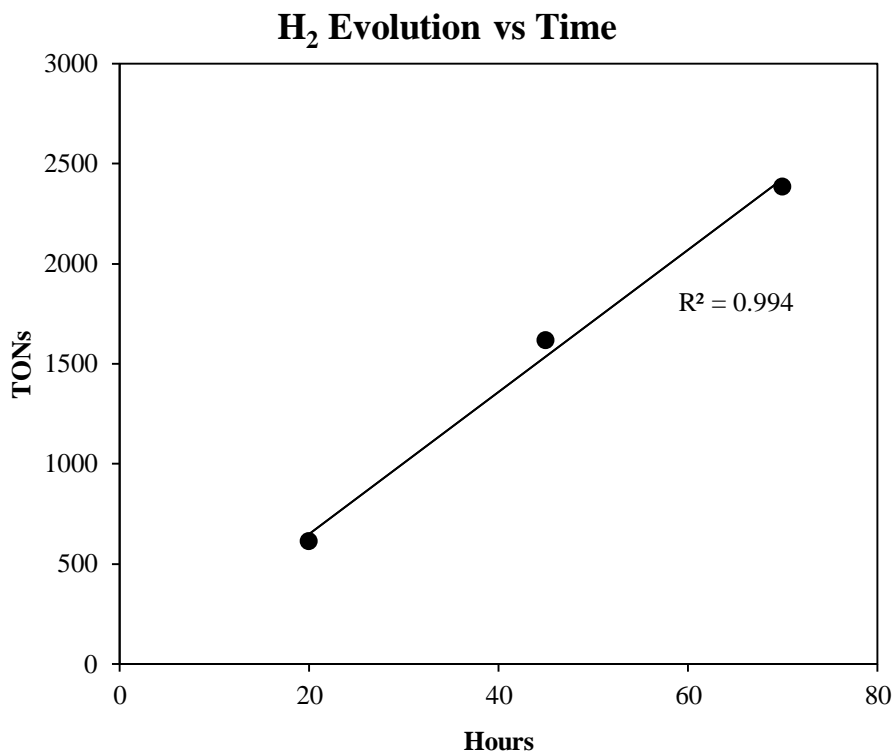
Figure 27. Hydrogen production from a photolysis experiment containing **1** (1.5 x 10^{-6} M), fluorescein (1.4 mM), and TEA (5% v/v) in 1:1 EtOH/H$_2$O at pH 12 over 70 hours.

In order to determine the optimal conditions for hydrogen evolution, the concentration of catalyst was varied while the concentration of fluorescein and TEA were held constant. It was found that while the volume of H$_2$ evolved generally decreased with the concentration of **1**, the TONs increased. However, when the ratio of catalyst to chromophore became too low, the samples bleached and hydrogen evolution decreased

42

sharply.   It is suspected that this is caused by unimolecular decomposition of the fluorescein anion, which is generated by the reductive quenching of Fl* by TEA.[32]

Catalyst Concentration Study
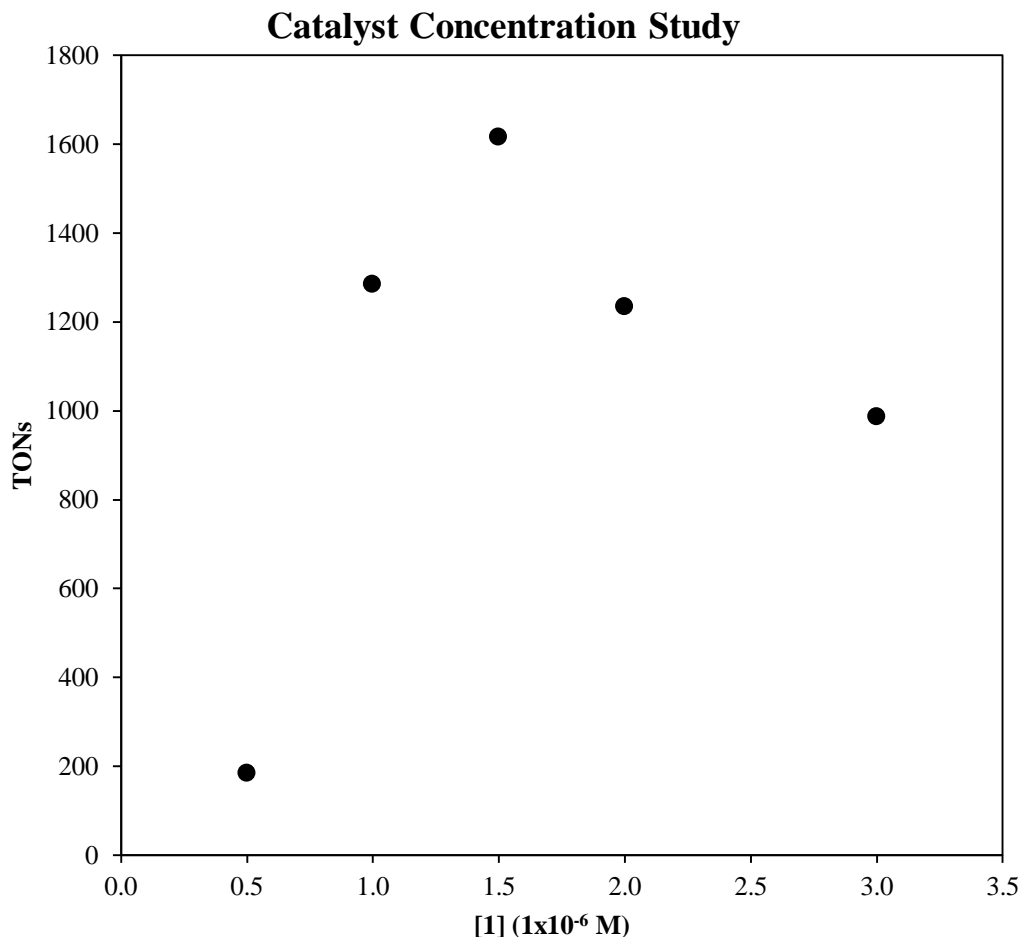
Figure 28. Hydrogen evolution by systems containing various amounts of **1** with fluorescein (1.4 mM), TEA (5% v/v) in 1:1 EtOH/H$_2$O at pH 12 after 45 hours.

The literature indicates that hydrogen evolution will increase with photosensitizer concentration; however, that trend was not observed in this photosystem.[22]   Hydrogen generation peaks when fluorescein is at a concentration of 1.2 mM (Fig. 28).   It is suspected that at higher concentrations of chromophore, the fluorescein is decomposing through a self-quenching mechanism.
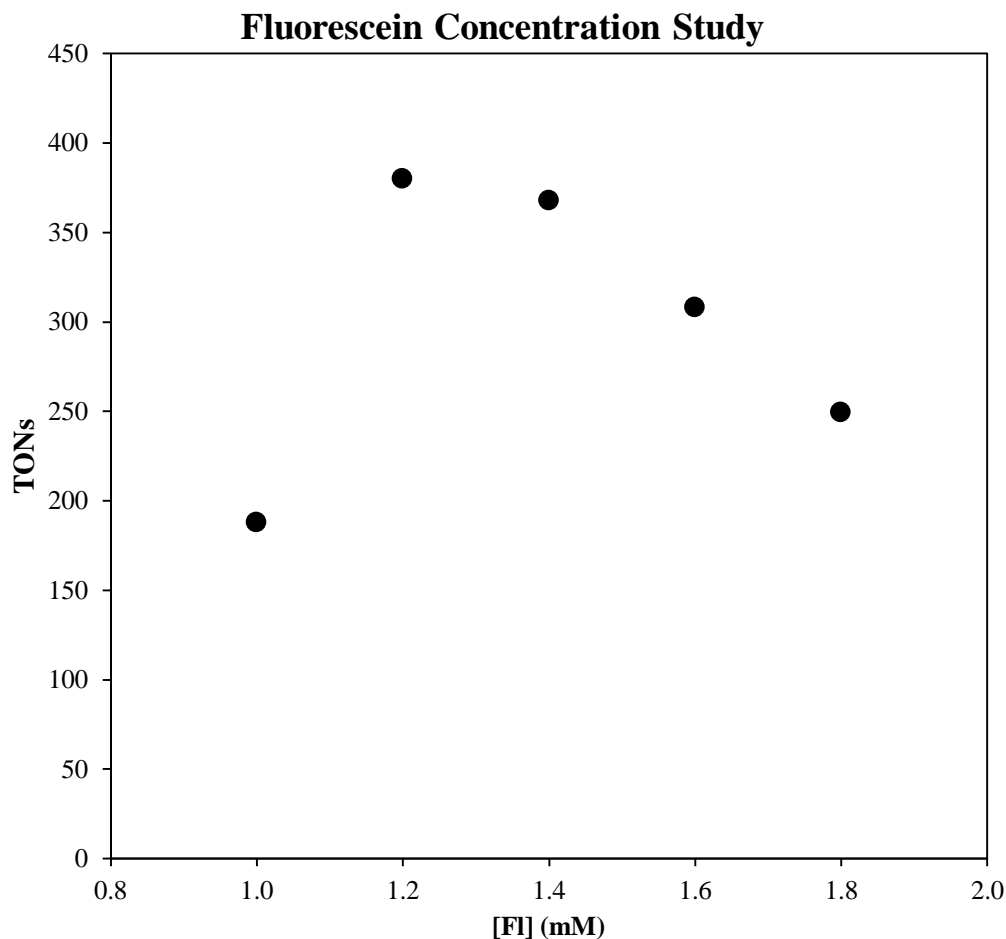
Figure 29. Turnover numbers of H_2 after completion of photolysis experiments containing **1** (1×10^{-5} M), TEA (5% v/v) in 1:1 EtOH/H_2O at pH 12 containing various amounts of fluorescein.

Photochemistry experiments were run with **1** and **2** under identical experimental conditions in order to directly compare their ability to generate hydrogen under those conditions. This type of experiment is effective for comparison, but it does not accurately reflect the photocatalytic properties of **2**. The addition of the electron withdrawing group to **2** resulted in a lower catalytic potential for catalytic proton reduction and therefore a lower overpotential. Because **2** reduces protons at a less cathodic potential than **1**, it is predicted that **2** will function better in a photosystem employing a less reducing chromophore. It was found that in a photocatalytic system

using fluorescein and TEA, **2** evolved significantly less hydrogen than **1** under identical conditions. After 24 hours, **1** produced 920 equivalents of hydrogen with respect to catalyst, while **2** had produced 100 equivalents. This discrepancy was expected based on the differing electrochemical properties of the two compounds.

In order to further evaluate the kinetics of the photosystem containing **1**, fluorescein, and TEA, fluorescence quenching experiments were performed. Fluorescence is the emission of a photon that occurs when an excited electron in an atom or molecule relaxes to its ground state. In the presence of a second molecule, fluorescence can be diminished due to energy transfer between the two systems, which is known as quenching. In relation to the photocatalytic system previously described, fluorescence quenching studies give insight to the kinetics of the electron transfer between the chromophore and the catalyst or the sacrificial donor. Quenching can proceed via two pathways: static and dynamic. In static quenching, a non-fluorescent complex is formed by interactions between the two compounds. In dynamic quenching, also called collisional quenching, fluorescence is diminished by electron transfer from the excited chromophore into the quencher molecule.[33] This interaction is dependent on collisions between the two molecules; therefore it is limited by diffusion. The relationship between the concentration of the quencher and the change in fluorescence intensity in dynamic quenching systems is given by the Stern-Volmer equation:

$$\frac{I_o}{I} = 1 + k_q \tau_o [Q]$$

In this equation, I_o is the initial fluorescence intensity of the chromophore in the absence of quencher; I is the intensity after the quencher is added; Q is the concentration of quencher; k_q is the bimolecular quenching constant and τ_o is the fluorescence lifetime of

the chromophore. If the quenching is proceeding via a dynamic mechanism, then the relationship between I_o/I and $[Q]$ will be linear and the value of k_q can be determined by plotting those two variables against one another. The quenching constant, k_q, gives insight to both the efficiency and mechanism of electron transfer. If k_q exceeds the diffusion limit, which varies with solvent viscosity but can be approximated as 1×10^{10} $M^{-1}s^{-1}$, then the fluorescence quenching is presumed to be occurring by mixture static and dynamic quenching interactions, rather than just the dynamic pathway. In addition, it is necessary to perform the experiments under air-free conditions because molecular oxygen is known to quench most chromophores.

It was found that **1** quenches the fluorescence of fluorescein under 1:1 EtOH/H_2O solvent conditions (Fig. 30), as well as in solvent mixtures containing acetonitrile and water. Using the Stern-Volmer relationship, the value of k_q was determined to be 6×10^7 $M^{-1}s^{-1}$ (Fig. 31). The plot of I_o/I_f verses catalyst concentration showed a linear relationship, which indicates that the quenching of fluorescein by **1** is proceeding by a dynamic quenching mechanism. A mixture of static and dynamic quenching would result in a non-linear relationship.
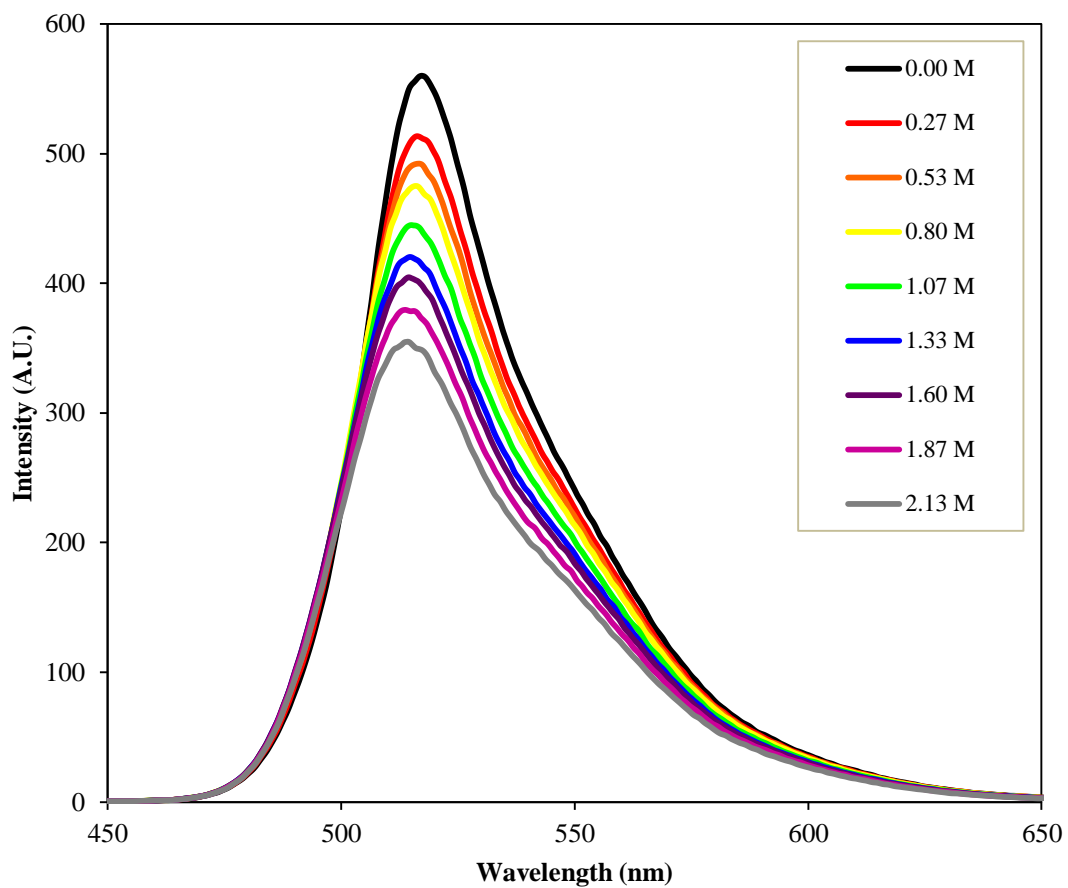
Figure 30. Fluorescence quenching of 1×10^{-5} M fluorescein in 1:1 EtOH/H$_2$O by **1**.
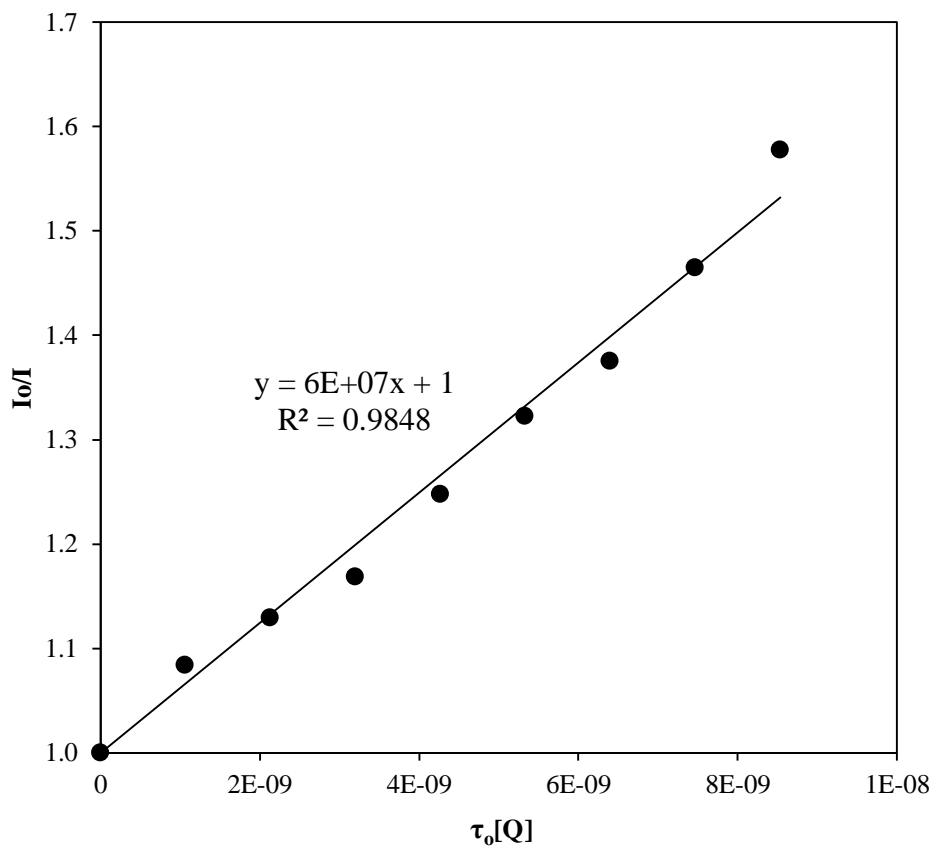
Figure 31. Stern-Volmer plot of the experiment shown in Fig. 30 which shows a linear relationship between fluorescence quenching and the concentration of **1**.

Triethylamine (TEA) is known to quench the fluorescence of fluorescein. In the literature, the quenching constant for the quenching of fluorescein by TEA was found to be 5.20×10^7 $M^{-1}s^{-1}$ in 1:1 CH_3CN/H_2O solvent conditions.[30] Our study in 1:1 $EtOH/H_2O$ found the value of k_q to be 3.0×10^8 $M^{-1}s^{-1}$ (Fig. 32). It is suspected that this discrepancy is due to the different viscosities of the solvents, which affects the frequency of collisions between fluorescein and TEA, or alternatively due to the difference in fluorescence lifetime between the two solvent conditions. The value of k_q is greater for TEA than it is for **1**, which indicates that the electron transfer is faster between TEA and fluorescein.

48
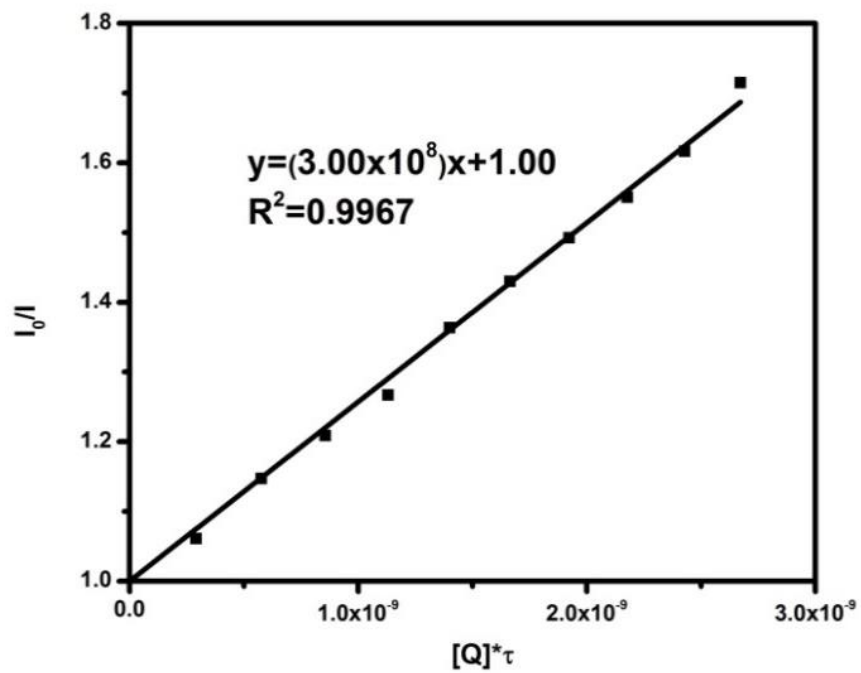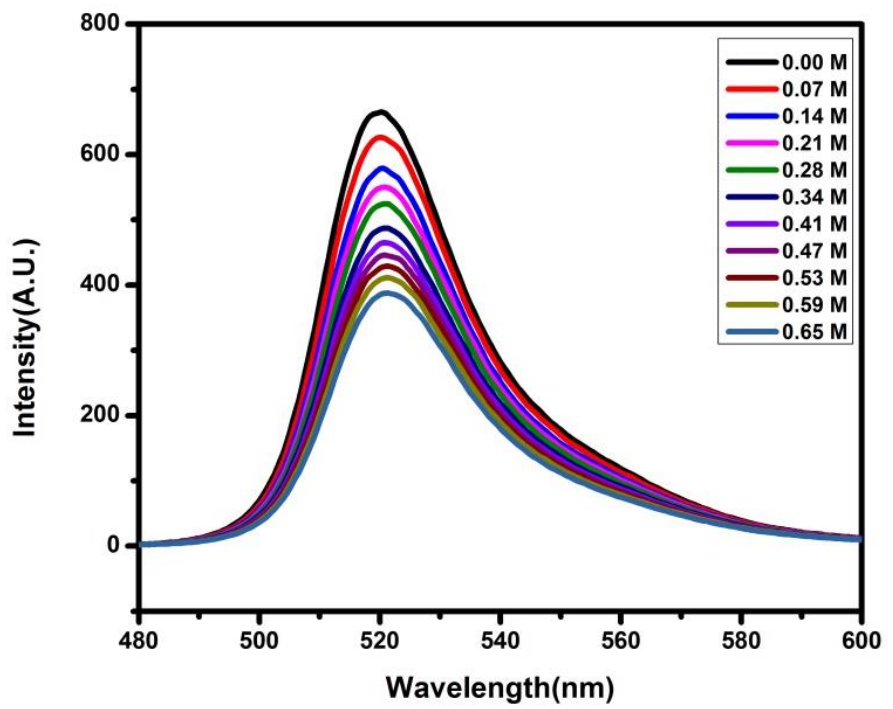
Figure 32. Quenching of fluorescein (1×10^{-5} M) by TEA in 1:1 EtOH/H$_2$O solution (top). The Stern-Volmer plot shows a linear relationship (bottom).

Conclusions

A highly active electrocatalyst suitable for photocatalytic proton reduction has been identified. In 1:1 CH_3CN/H_2O solutions, **1** exhibits an i_c/i_p of 15.6 and an overpotential of 800 mV, making it highly suitable for use in a photocatalytic system for hydrogen evolution. Controlled potential coulometry shows that **1** is capable of electrocatalytically evolving H_2 from citrate-buffered aqueous solutions at a rate of 23.0 equivalents per hour with respect to catalyst and a faradaic efficiency of 98%. Cyclic voltammetry of complex **2**, a nitro-substituted derivative of **1**, also shows catalytic activity in CH_3CN and it operates at a much lower overpotential.

When paired with fluorescein as a photosensitizer, **1** exhibits photocatalytic hydrogen production in excess of 2,400 equivalents with respect to catalyst. This system is highly active compared to other noble metal free photocatalytic systems. The system functions optimally at pH 12 with high concentrations of TEA (5% v/v). Fluorescence quenching experiments indicate that the electron transfer between fluorescein and **1** is occurring through a dynamic quenching mechanism. Hydrogen evolution was observed by **2** in the same photocatalytic system; however, the yield of H_2 was significantly lower.

The electrochemical properties of complex **1** can be tuned by adding electron withdrawing and electron donating groups to the ligand backbone. The addition of a single nitro group to the ligand decreases the reduction potential by 440 mV. It is predicted that by adding different electron withdrawing groups, such as halogens, or electron donating groups, such as a t-butyl groups, the catalyst can be tuned to work with different chromophores in a variety of photocatalytic systems for hydrogen evolution.

In addition to their stability in water, a key benefit of these complexes is that the ligand can be easily modified with different functional groups to adjust their electrochemical properties. As a result, these iron complexes can be tuned for specific purposes, such as use with a certain chromophore. The ease with which the ligand backbone can be modified also means that these complexes could potentially be tethered to a TiO_2 semiconductor for the development of a heterogeneous photocatalytic system, as described in Fig. 8. Due to their versatility, efficiency, and activity, these iron polypyridyl complexes represent a promising advance in the development of noble metal-free systems for photocatalytic hydrogen generation.

Appendix

Figure A1: ^{1}H-NMR of L$_1$
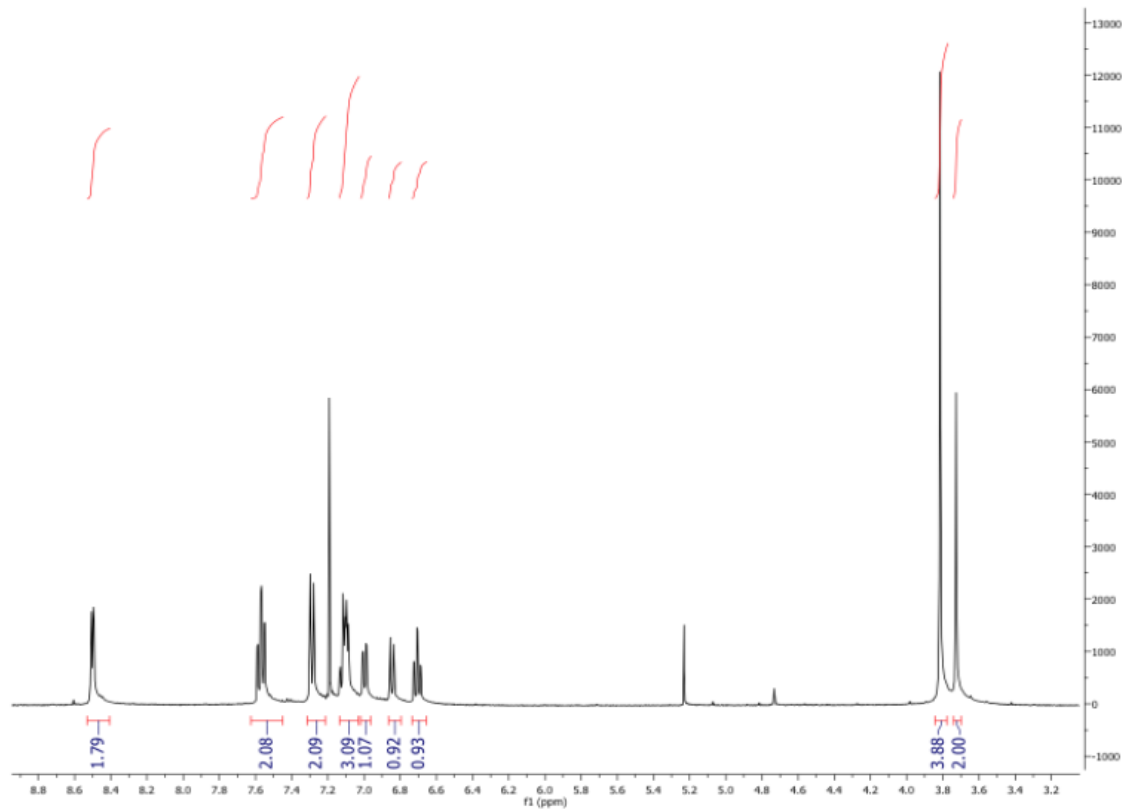
^{1}H-NMR spectrum of **L$_1$** in CDCl$_3$ with integrations shown in blue.

Figure A2: High Resolution Mass Spectrometry of 1
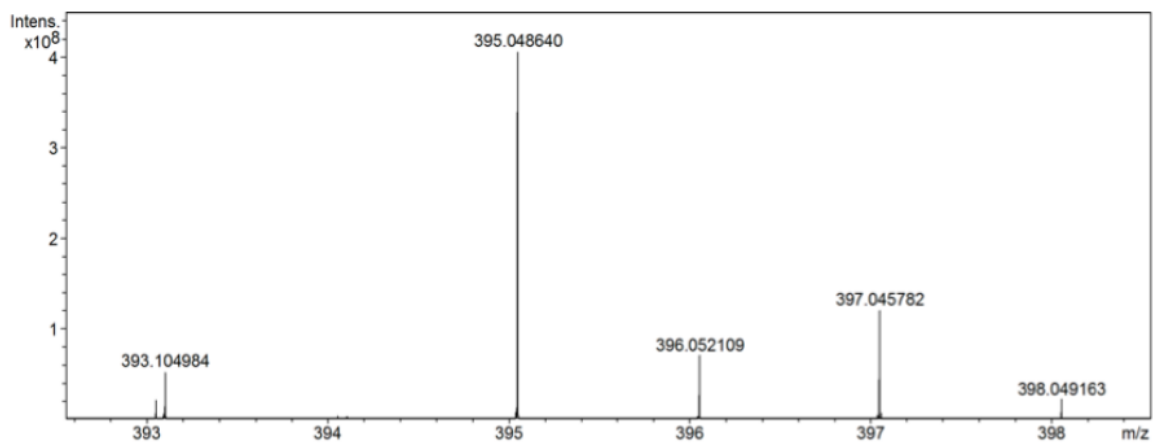
High-resolution mass spectrum of **1** in H_2O/MeOH. Analysis was completed through positive electrospray ionization on a Burker 12 Tesla APEX-Qe FTICR-MS with an Apollo II ion source. The molecular ion detected was charged due to the dissociation of a chlorine during testing. The expected molecular ions were observed with a difference of less than 1 ppm.

Figure A3: ORTEP Diagram of 1

ORTEP diagram of **1**. Fe (orange), O (red), Cl (green), N (blue), C (black). Ellipsoids are at the 50% probability level. Hydrogen atoms have been omitted for clarity.

Table 1 Bond lengths(Å) and angles (°) for **1**

Fe(1)-O(1)	1.896(2)
Fe(1)-N(3)	2.179(3)
Fe(1)-N(1)	2.198(3)
Fe(1)-N(2)	2.250(3)
Fe(1)-Cl(2)	2.2729(9)
Fe(1)-Cl(1)	2.3425(9)
O(1)-Fe(1)-N(3)	162.08(10)
O(1)-Fe(1)-N(1)	85.67(10)
N(3)-Fe(1)-N(1)	85.05(10)
O(1)-Fe(1)-N(2)	88.94(9)
N(3)-Fe(1)-N(2)	74.01(10)
N(1)-Fe(1)-N(2)	76.61(10)
O(1)-Fe(1)-Cl(2)	99.89(7)
N(3)-Fe(1)-Cl(2)	96.13(8)
N(1)-Fe(1)-Cl(2)	94.74(8)
N(2)-Fe(1)-Cl(2)	167.23(7)
O(1)-Fe(1)-Cl(1)	98.14(7)
N(3)-Fe(1)-Cl(1)	87.82(7)
N(1)-Fe(1)-Cl(1)	166.99(8)
N(2)-Fe(1)-Cl(1)	90.97(7)
Cl(2)-Fe(1)-Cl(1)	96.84(3)
C(19)-O(1)-Fe(1)	131.0(2)
C(8)-N(3)-Fe(1)	115.6(2)

Table 2 X-ray Crystallography Selected Data for **1**

Empirical Formula	$C_{19}H_{18}Cl_2FeN_3O$
fw (g/mol)	431.11
color/habit	dark blue plate
T (K)	100(2)
space group	*P21/n*
Z	4
a (Å)	14.9012(2)
b (Å)	7.05310(10)
c (Å)	17.5715(3)
α (deg)	90
β (deg)	103.0850(10)
γ (deg)	90
V (Å^3)	1798.81(5)
Final R-indices ($I>2\sigma$)	0.0408, 0.0996
Final R-indices (all data)	0.0487, 0.1062
GOF	1.027
No. reflections measured	17916
No. of independent reflections	3148
R_{int}	0.0693

Figure A3: ^{1}H-NMR of L$_2$
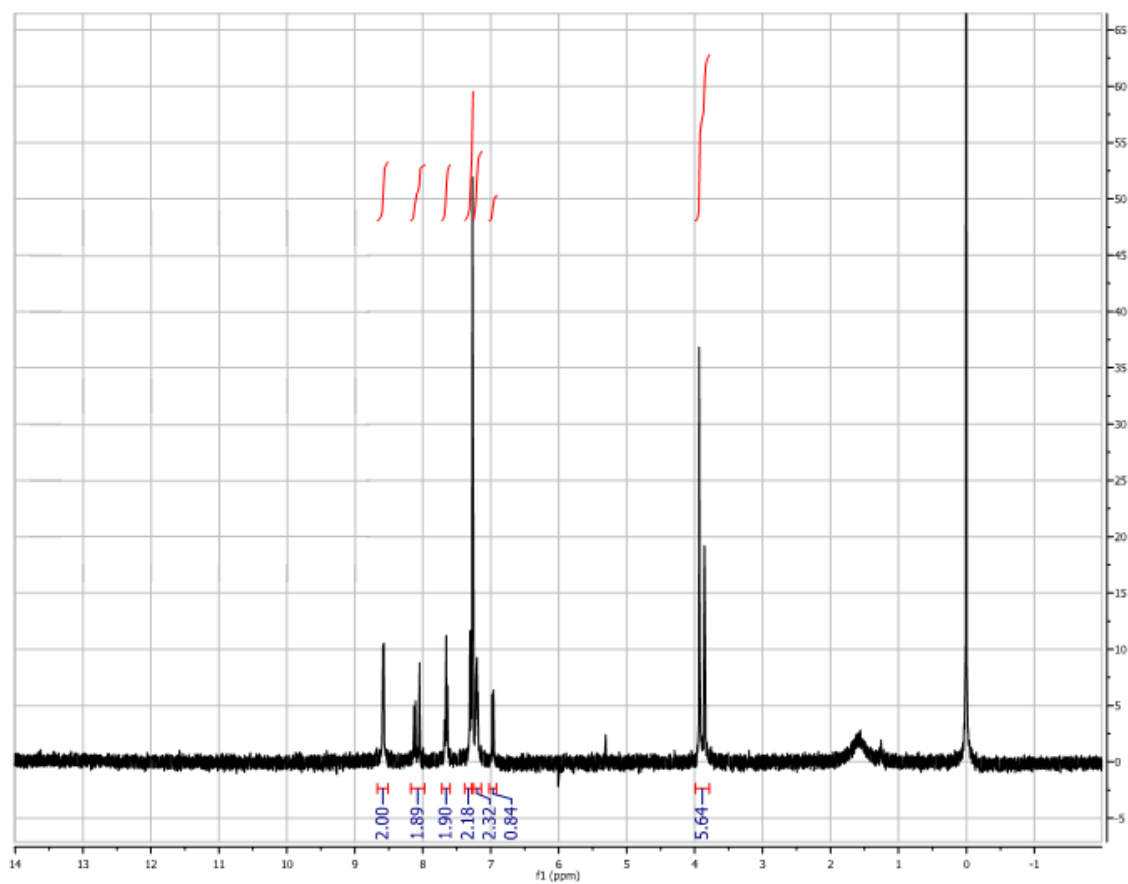
^{1}H-NMR spectrum of **L$_2$** in CDCl$_3$ with integrations shown in blue.

Figure A4: High Resolution Mass Spectrometry of 2
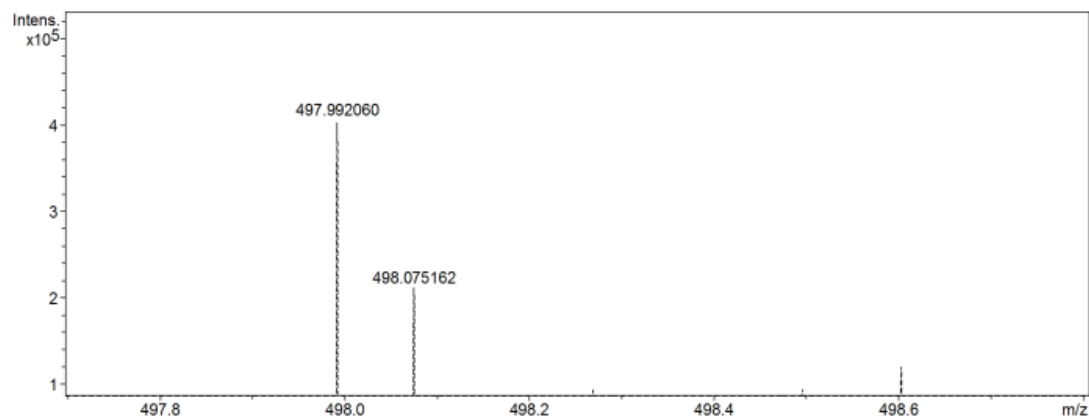
High-resolution mass spectrum of **2** in H_2O/MeOH. The molecular ion detected was charged due to the association of a sodium ion.

References

(1) *Climate Change 2013: The Physical Science Basis*. *Contribution of Working Group I to the Fifth Assessment Report of the Intergovernmental Panel on Climate Change*. Stocker, T. F.; Quin, D.; Plattner, G.; Tignor, M. M. B.; Allen, S. K.; Boschung, J.; Nauels, A.; Xia, Y.; Bex, V.; Midgley, P. M., Eds.; Cambridge University Press, Cambridge UK, **2013.**

(2) Oreskes, N. *Science*, **2004**, 306, 1686.

(3)National Aeronautics and Space Administration. *GISS Surface Temperature Analysis Data;* http://data.giss.nasa.gov/gistemp/ , (accessed March 29, 2015).

(4) Callendar, G. S. *Quarterly Journal of the Royal Society of Meteorology,* **1938**, 64, 223-240.

(5) Woodwell, G. M.; Hobbie, J. E.; Houghton, R. A.; Meillo, J. M.; Moore, B.; Peterson, B. J.; Shaver, G. R. *Science*, **1983**, 222, 1081-1086.

(6) Keeling, R. F.; Walker, S. J.; Piper, S. C.; Bollenbacher, A. F.; *Atmospheric CO2 Concentrations Derived from In Situ Air Measurements at Mauna Loa Observatory, Hawaii.* Scripps Institute of Oceanography CO_2 Program, http://scrippsco2.ucsd.edu/research/atmospheric_co2, (Accessed 3/31/2015).

(7) Likens, G. E.; Bormann, F. H., "Acid Rain: A Serious Regional Environmental Problem", *Science*, **1974**, *184*, 1176-1179.

(8) Pacyna, E. G.; Pacyna, J. M.; Steenhuisen, F.; Wilson, S. *Atmospheric Environment,* **2006,** *40*, 4048-4063.

(9) Harris, H. H.; Pickering, I. J.; George, G. N. *Science,* **2003,** 301, 1203.

(10) World Health Organization, "Air Quality Guidelines for Particulate Matter, Ozone, Nitrogen Dioxide, and Sulfur Dioxide: Global Update 2005", **2006,** http://www.euro.who.int/__data/assets/pdf_file/0005/78638/E90038.pdf?ua=1, (Accessed 4/12/2015).

(11) U.S. Global Change Research Program. *Global Climate Change Impacts in the United States* . **2009** Karl, T.R., J.M. Melillo, and T.C. Peterson (eds.) United States Global Change Research Program. Cambridge University Press, New York, NY, USA.

(12) Loomis, D.; Grosse, Y.; Lauby-Scretan, B.; El Ghissassi, F.; Bouvard, V.; Benbrahim-Tallaa, L.; Guha, N.; Baan, R.; Mattock, H.; Straif, K.; *The Lancet Oncology,* **2013**, 14 (13), 1262-1263.

(13) U.S. Energy Information Administration, *Levelized Cost and Levelized Avoided Cost of New Generation Resources in the Annual Energy Outlook 2014*, **2014**.

(14) U.S. Energy Information Administration, *International Energy Statistics*, http://www.eia.gov/countries/data.cfm, (accessed March 31, 2015).

(15) Lewis, N. S.; Nocera, D. G. *Proc. Natl. Acad. Sci. U.S.A.* **2006**, 103, 15729.

(16) Smallwood, K. S. *Wildlife Society Bulletin*, **2013**, 37, 19-33.

(17) Dauble, D. D.; Hanrahan, T. P.; Geist, D. R.; Parsley, M. J. *North American Journal of Fisheries Management*, **2003,** 23, 641-659.

(18) Lopez, A.; Roberts, B.; Heimiller, D.; Blair, N.; Porro, G. *U.S. Renewable Energy Technical Potentials: A GIS-Based Analysis*, **2012**, http://www.nrel.gov/gis/re_potential.html, (Accessed 3/31/2015).

(19) Wang, K.; Jiang, K.; Chung, B.; Ouchi, T.; Burke, P. J.; Boysen, D. A.; Bradwell, D. J.; Kim, H.; Muecke, U.; Sadoway, D. R. *Nature*. **2014**, 514, 348-350.

(20) U.S. Department of Energy, *Grid Energy Storage*, **2013**.

(21) Benson, E. E.; Kubiak, C. P.; Sathrum, A. J.; Smieja, J. M. *Chem. Soc. Rev.* **2008,** 38, 89-99.

(22) Eberle, U.; Von Helmolt, R. *Energy & Env. Sci.* **2010**, 3, 689-99.

(23) Graetz, J. *Chem. Soc. Rev.* **2008,** 38, 73-82.

(24) Mayilmurugan, R.; Visvaganesan, K.; Suresh, E.; Palaniandavar, M. *Inorg. Chem.* **2009**, *48*, 8771-8783.

(25) Viswanathan, R.; Palaniandavan, M.; Blasubramanian, T.; Muthiah, P. T. *Inorg. Chem.* **1998**, 37, 2943-2951.

(26) Roberts, A. S.; Bullock, R. M. *Inorg. Chem.* **2013**, 52, 3823-3835.

(27) Rose, M. J.; Gray, H. B.; Winkler, J. R. *J. Am. Chem. Soc.* **2012,** 1324, 8310-8313.

(28) McNamara, W. R.; Han, Z.; Alperin, P. J.; Brennessel, W. W.; Holland, P. L.; Eisenberg, R. *J. Am. Chem. Soc.* **2011**, 133, 15368-15371.

(29) Imamura, M. *Bull. Chem. Soc. Jpn.* **1958**, 31, 962-969.

(30) Han, Z.; McNamara, W. R.; Eum, M. S.; Holland, P. L.; Eisenberg, R. *Angew. Chem. Int. Ed.* **2012**, 51, 1667-1670.

(31) Jing, X.; Wu, P.; Liu, X.; Yang, L.; He, C.; Duan, C. *New J. Chem.* **2015**, 39, 1051-1059.

(32) McCormick, T. M.; Calitree, B. D.; Orchard, A.; Kraut, N. D.; Bright, F. V.; Detty, M. R.; Eisenberg, R. *J. Am. Chem. Soc.* **2010**, 132, 15480 – 15483.

(33) Lakowicz, J. R. *Principles of Fluorescence Spectroscopy*, 3rd ed.; Springer, New York, **2011**.